

Subaru High- z Exploration of Low-Luminosity Quasars (SHELLQs). XXV. Large-scale environments of low-luminosity quasars at $z \sim 6$ traced by Ly α emitters

Junya Arita,^{1*} Nobunari Kashikawa,^{1,2} Yoshiki Matsuoka,³ Masafusa Onoue,^{4,5} Michael A. Strauss,⁶ Kentaro Koretomo,¹ Yoshihiro Takeda,¹ Ryo Emori,¹ Wanqiu He,⁷ Hiroki Hoshi,¹ Masatoshi Imanishi,^{7,8} Rikako Ishimoto,¹ Kei Ito,^{9,10} Kazushi Iwasawa,¹¹ Satoshi Kikuta,¹ Yongming Liang,^{7,12} Camryn L. Phillips,⁶ Shunta Shimizu,¹ John D. Silverman,^{1,5,13,14} Yoshiki Toba,^{3,15,16} Takehiro Yoshioka¹

¹Department of Astronomy, School of Science, The University of Tokyo, 7-3-1, Hongo, Bunkyo, Tokyo 113-0033, Japan

²Center for the Early Universe, The University of Tokyo, 7-3-1 Hongo, Bunkyo, Tokyo, 113-0033, Japan

³Research Center for Space and Cosmic Evolution, Ehime University, 2-5 Bunkyo-cho, Matsuyama, Ehime 790-8577, Japan

⁴Waseda Institute for Advanced Study (WIAS), Waseda University, 1-21-1, Nishi-Waseda, Shinjuku, Tokyo 169-0051, Japan

⁵Kavli Institute for the Physics and Mathematics of the Universe (Kavli IPMU, WPI), UTIAS, Tokyo Institutes for Advanced Study, University of Tokyo, Chiba, 277-8583, Japan

⁶Department of Astrophysical Sciences, Princeton University, 4 Ivy Lane, Princeton, NJ 08544, USA

⁷National Astronomical Observatory of Japan, Mitaka, Tokyo 181-8588, Japan

⁸Department of Astronomical Science, Graduate University for Advanced Studies (SOKENDAI), Mitaka, Tokyo 181-8588, Japan

⁹Cosmic Dawn Center (DAWN), Copenhagen, Denmark

¹⁰DTU Space, Technical University of Denmark, Elektrovej 327, DK2800 Kgs. Lyngby, Denmark

¹¹ICREA and Institut de Ciències del Cosmos, Universitat de Barcelona, IEEC-UB, Martí i Franquès, 1, 08028 Barcelona, Spain

¹²Institute for Cosmic Ray Research, The University of Tokyo, 5-1-5 Kashiwanoha, Kashiwa, Chiba 277-8582, Japan

¹³Center for Data-Driven Discovery, Kavli IPMU (WPI), UTIAS, The University of Tokyo, Kashiwa, Chiba 277-8583, Japan

¹⁴Center for Astrophysical Sciences, Department of Physics & Astronomy, Johns Hopkins University, Baltimore, MD 21218, USA

¹⁵Department of Physical Sciences, Ritsumeikan University, 1-1-1 Noji-higashi, Kusatsu, Shiga 525-8577, Japan

¹⁶Academia Sinica Institute of Astronomy and Astrophysics, 11F of Astronomy-Mathematics Building, AS/NTU, No.1, Section 4, Roosevelt Road, Taipei 10617, Taiwan

Accepted XXX. Received YYY; in original form ZZZ

ABSTRACT

High- z quasars are believed to reside in massive dark matter haloes (DMHs), suggesting that they reside in galaxy overdense regions. However, previous observations have shown a range of environments around them. The previous targets are limited to bright quasars ($M_{1450} \lesssim -25$), for which photoevaporation may hinder galaxy formation in their vicinity. Here, we present Subaru/Hyper-Suprime Cam observations of the environments of four low-luminosity quasars ($-24 < M_{1450} < -22$) at $z \sim 6.18$, which are expected to have a smaller photoevaporation effect. We detect Lyman α emitters (LAEs) around them with narrowband NB872 imaging, and measure the local LAE overdensity. One quasar (J0844–0132) resides in an overdense region ($\delta_{\text{LAE}} = 3.77 \pm 0.97$), whereas the other three fields are consistent with normal fields. The result is confirmed over the proximity zone of each quasar, suggesting that the diverse environment around quasars is independent of photoevaporation. We find no significant correlation between the LAE overdensities and the properties of host galaxies and supermassive black holes. Our quasars have host stellar mass measurements from JWST, allowing us to compare them with the LAE overdensity around galaxies without quasar activity with comparable stellar masses. We find that the LAE overdensity in the J0844–0132 field is stronger than that of galaxies with similar stellar mass at $z \sim 6$, while the other quasar fields show a comparable LAE overdensity.

Key words: quasars: general – large-scale structure of Universe – galaxies: high-redshift

1 INTRODUCTION

The emergence of supermassive black holes (SMBHs) within 1 Gyr after the Big Bang, as revealed by recent observations of quasars at $z \gtrsim 6$ (e.g. Mortlock et al. 2011; Bañados et al. 2018; Matsuoka et al. 2019a; Yang et al. 2020b; Wang et al. 2021 and Fan et al. 2023 for

review), is one of the intriguing mysteries in the early Universe. To explain their rapid growth, it is suggested that high- z quasars reside in massive dark matter haloes (DMHs) to reserve sufficient gas for mass growth (Volonteri & Rees 2006). This picture is supported by many cosmological simulations (e.g. Springel et al. 2005; Costa et al. 2014). However, observational evidence for this has been lacking due to the very low number density of high- z luminous quasars that can be identified by previous large surveys, which hinders us from measuring

* E-mail: jarita@astron.s.u-tokyo.ac.jp

their clustering, and thus constraining their DMH mass (e.g. [Martini & Weinberg 2001](#)). Measuring the statistically significant clustering signal of high- z quasars requires a wide and deep survey of the quasars themselves and their surrounding galaxies; however, such surveys have typically been very expensive.

Recently, [Arita et al. \(2023\)](#) measured the auto-correlation function of low-luminosity ($M_{1450} \lesssim -21$) quasars at $z \sim 6$. They found that their typical DMH mass is high, $\sim 10^{12.85} M_{\odot}$, near the massive end of the DMH mass function at $z \sim 6$, suggesting that quasars are born in rare high-density peaks. The result is supported by the cross-correlation analysis using bright quasars at $z \sim 6$ with their surrounding [O III] emitters observed by JWST/NIRCam slitless spectroscopy in Emission-line galaxies and Intergalactic Gas in the Epoch of Reionization (EIGER) program ([Eilers et al. 2024](#)) and A SPectroscopic survey of biased halos In the Reionization Era (ASPIRE) program ([Huang et al. 2026](#)). [Eilers et al. \(2024\)](#) and [Huang et al. \(2026\)](#) derived a minimum DMH mass of $10^{12.43} M_{\odot}$ and $10^{12.13} M_{\odot}$ using four bright quasars with 92 [O III] emitters and 25 bright quasars with 487 [O III] emitters, respectively. These studies also show that the bias parameter of quasars tends to increase as the redshift increases, which suggests that higher- z quasars reside in higher density peaks than lower- z quasars. In fact, previous statistical studies on the large-scale environments of quasars at $z < 4$ show that many of them reside in non-overdense regions ([Uchiyama et al. 2018, 2020](#); [Suzuki et al. 2024](#); [Shibata et al. 2025](#)). Contrary to the large-scale environment of the lower- z quasars, that of $z \sim 6$ quasars is highly biased, so these quasar fields must be traced by galaxy overdensities extending up to ~ 10 pMpc based on a cosmological simulation ([Overzier et al. 2009](#)). Understanding the environment of early quasars is essential to reveal the amount of gas fuelling SMBHs and the mechanism of gas accretion onto them (e.g. [Granato et al. 2004](#)), and also has significant implications for the onset of the mass-related coevolution between galaxies and SMBHs.

However, observational evidence of galaxy clustering around quasars at $z \sim 6$ is far from conclusive, with some studies reporting significant overdensity (e.g. [Zheng et al. 2006](#); [Utsumi et al. 2010](#); [Morselli et al. 2014](#); [Mignoli et al. 2020](#); [Wang et al. 2024](#); [Lambert et al. 2024](#)), while others find normal or even underdense environments (e.g. [Bañados et al. 2013](#); [Simpson et al. 2014](#); [Mazzucchelli et al. 2017](#); [Kikuta et al. 2017](#); [Goto et al. 2017](#)). Recent observations with JWST found a clear overdensity of [O III] emitters around $z \sim 6$ quasars ([Wang et al. 2023](#); [Kashino et al. 2023](#); [Champagne et al. 2025](#)), but the field of views (FoVs) are narrow, and the sample is still limited. The lack of clear evidence for galaxy overdensities around $z \sim 6$ quasars is a real challenge to our current paradigm of early black hole growth.

One possible reason why galaxy overdensities around $z \sim 6$ quasars are not always seen is feedback by the quasars themselves on the surrounding gas. Photoionization heating by intense UV radiation from quasars could heat the collapsed gas in a galactic halo and inhibit gas cooling ([Barkana & Loeb 1999](#)), suppressing star formation and delaying galaxy growth against galaxy self-shielding. Here, we call the intense photoionization heating possible to hinder the star formation activity of the surrounding galaxies by quasar photoevaporation. Some observations have found evidence of the effect at lower- z ([Kashikawa et al. 2007](#); [Bañados et al. 2018](#); [Uchiyama et al. 2019](#)). The effect of the photoevaporation is stronger in more luminous quasars. An ionized region around quasars generated by their own radiation is called the proximity zone ([Cen & Haiman 2000](#)), and its size R_p , which depends on quasar luminosity, can be recognized as the scale over which photoevaporation works (e.g. [Suzuki et al. 2025](#)). Most previous studies of galaxy overdensities around

quasars have focused on scales within R_p , which is typically 1.73 pMpc at $M_{1450} = -25$ ([Ishimoto et al. 2020](#)), due to the limited FoV of the instruments up to a few pMpc (e.g. [Willott et al. 2005](#); [Zheng et al. 2006](#); [Kim et al. 2009](#); [Bañados et al. 2013](#); [Mazzucchelli et al. 2017](#); [Mignoli et al. 2020](#)). These studies investigate highly limited areas in quasar fields, probing only dozens of arcmin² around bright quasars, where the photoevaporation effect can suppress star formation, decreasing the number of galaxies observed despite the presence of an underlying massive halo. The quasar photoevaporation, in principle, is a serious consideration for understanding the intrinsic quasar DMH mass and environment in the early universe. The intrinsic galaxy clustering strength can best be measured in regions outside of R_p and inside the typical cross-correlation scale of galaxies and quasars, which requires investigating the less luminous quasar fields than ever.

To minimize the effect, we investigate the fields of low-luminosity quasars whose expected proximity zone sizes are sufficiently small. We select the low-luminosity quasars discovered by the Subaru High- z Exploration of Low-Luminosity Quasars (SHELLQs; [Matsuoka et al. 2016](#)) project with systemic redshifts based on emission lines other than the Ly α emission line. Their absolute magnitudes are $-24 < M_{1450} < -22$, which is $\gtrsim 2$ mag fainter than those of bright quasars investigated in previous studies. Many studies have found that the DMH mass and thus presumably the corresponding galaxy overdensity are independent of M_{1450} at low- z ([Croom et al. 2005](#); [Shen et al. 2009](#)) and $z \sim 6$ ([Arita et al. 2023](#)), suggesting that targeting low-luminosity quasars does not result in examining a skewed environment. Moreover, the targeted quasars have been observed photometrically and spectroscopically by JWST (GO 1967, PI: M. Onoue), which provides their important host galaxy properties of stellar mass (M_*) ([Ding et al. 2023, 2025](#)) and star formation rate (SFR) ([Phillips et al. 2025](#)) and SMBH properties of SMBH mass and Eddington ratio (Onoue et al. in prep.). We use Hyper Suprime-Cam (HSC; [Miyazaki et al. 2018](#); [Komiyama et al. 2018](#); [Kawanomoto et al. 2018](#); [Furusawa et al. 2018](#)) on the Subaru Telescope whose diameter corresponds to roughly 220 cMpc at $z \sim 6$. HSC has a series of narrowband filters, including NB872 ($\lambda_c = 8721 \text{ \AA}$, FWHM = 67 \AA), which corresponds to Ly α emission at $z = 6.174 \pm 0.028$. In this paper, we, for the first time, present the low-luminosity quasar environments at $z \sim 6$ traced by Ly α emitters (LAEs), generally young low-mass galaxies, and the relation between LAE overdensity and the quasar properties.

This paper is structured as follows. The details of the observations and LAE selection are described in Sec. 2, and their results are shown in Sec. 3. In Sec. 4, we discuss the environment of low-luminosity quasars by comparing that of bright quasars investigated in the previous studies and the relation between the quasar environment and quasar properties. Finally, we summarize this paper in Sec. 5. We adopt a flat Λ cold dark matter cosmology with $h = 0.7$, $\Omega_m = 0.3$ throughout this paper. All magnitudes in this paper are presented in the AB system ([Oke & Gunn 1983](#)). The notations of cMpc and pMpc are used to indicate the comoving and physical scales, respectively.

2 OBSERVATIONS

We select four low-luminosity ($M_{1450} > -24$) quasars in the SHELLQs project: HSC J084408.61–013216.5, HSC J091833.17+013923.4, HSC J142517.72–001540.8, and HSC J151248.71+442217.5 (hereafter J0844–0132, J918+0139, J1425–0015, and J1512+4422), to investigate their environment using the surrounding LAEs. These quasars have accurate systemic

redshifts of $z \sim 6.18$, whose Ly α emission can be covered by NB872. The quasars were first discovered in the HSC Subaru Strategic Program (HSC-SSP) field (Aihara et al. 2018) and have already been confirmed by spectroscopic observations with the Faint Object Camera and Spectrograph (FOCAS; Kashikawa et al. 2002) on the Subaru telescope in SHELLQs. Their accurate redshift measurements based on [O III] $\lambda 5007$ emission lines are available from the JWST NIRSpec spectra (Onoue et al. in prep.). Their properties are summarized in Table 1.

2.1 Hyper Suprime-Cam imaging

The four quasar fields were included in the HSC-SSP Wide layer, so five broad bands (*grizy*) data are available. However, their exposure time is not sufficient (~ 1200 s), and the NB872 imaging was not performed. Therefore, we performed the additional Subaru/HSC observations centred on the quasars with two broadband filters (HSC-*i2* and HSC-*z*) and NB872 from December 2024 to July 2025 in queue mode. Their transmission curves are shown in Fig. 1. During the HSC observations, we performed dithering with a pre-defined 5-point dither pattern¹ and recommended dithering parameters ($120''$) for both RA and DEC directions to fill the gaps between the CCDs. Individual exposure times for the broad bands and NB872 are ~ 150 s and 900 s, respectively. Table 2 is the breakdown of total exposure time and seeing in the observations. In the data reduction, we combined the raw broadband data from HSC-SSP with that of our observation to improve the image depth. However, we note that HSC-*i2* data of the J0918+0139 and J1425-0015 fields are absent since the HSC-SSP used HSC-*i* instead of HSC-*i2*². The transmission curves of HSC-*i* and HSC-*i2* are slightly different, so we did not include the data of the HSC-*i* in HSC-SSP. The data were processed with `hscpipe 8.5.3` (Bosch et al. 2018)³, which can create calibrated images and object catalogues from raw HSC data. In `hscpipe`, the astrometry and photometry are calibrated based on Pan-STARRS DR1 (Chambers et al. 2016). We use NB872 as the first reference filter for the source detection. In this study, we use `ext_convolved_ConvolvedFlux_2_4_5_instFlux` in the photometry catalogue, which is the aperture flux measured within the $1''.5$ diameter aperture after an aperture correction. We use some flags to exclude objects that are affected by saturated pixels or bad pixels, as summarized in Table 3.

In `hscpipe`, the magnitude zeropoints of the coadded images are set to 27.0 mag/ADU. However, the absence of the NB872 data in the calibration catalogue can cause a non-negligible error in the magnitude zeropoint. Therefore, we correct the magnitude zeropoint of the NB872 image assuming that the magnitude zeropoint of HSC-*z* is adequately corrected in `hscpipe` and that the stars in the fields meet $\langle z - NB872 \rangle = 0$. The validity of the latter assumption is confirmed by computing the $z - NB872$ colour of stars in X-shooter Spectral Library Data Release 3 (Verro et al. 2022) based on their spectra. For the magnitude zeropoint calibration, we select stars from the photometry catalogue using the seventeenth data release of the Sloan Digital Sky Survey (Abdurro'uf et al. 2022), which classifies stars based on their morphology. We measure the median colours of $z - NB872$ of the stars in the individual fields and correct the magnitude zeropoint.

¹ <https://www.naoj.org/Observing/queue/pidoc/proposals.html#dithering>

² HSC-*i* was replaced by HSC-*i2* on Feb. 2016.

³ https://hsc.mtk.nao.ac.jp/pipedoc_e/

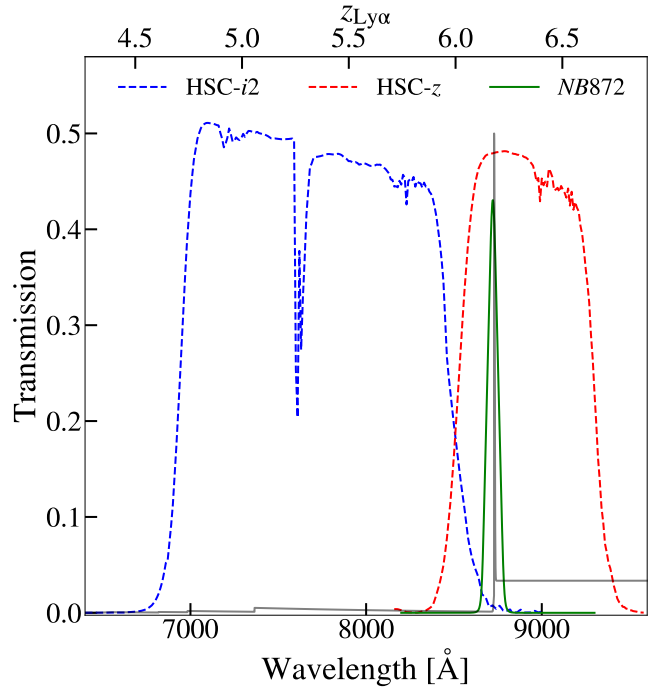


Figure 1. Filter transmission curves in this study. The red and blue dashed lines represent the transmission curves of HSC-*i2* and HSC-*z*, respectively. The green solid line is the transmission curve of NB872. These transmission curves include the atmospheric absorption. The grey line shows a model spectrum of an LAE at $z = 6.18$ generated by the procedure in Sec. 2.2 with $\alpha = -2$ and $EW_0 = 15$ Å. The upper x -axis displays the redshift of Ly α .

We determine mask regions around bright stars in addition to those defined in `hscpipe`. We use Gaia Data Release 3 (DR3) (Gaia Collaboration et al. 2016, 2023) to select bright stars ($G_{\text{Gaia}} < 18$, where G_{Gaia} is the G -band magnitude from Gaia DR3) in the fields. We apply masks centred on the stars to the field, whose radii r are determined by the following equation (Coupon et al. 2018):

$$r ['] = \begin{cases} 708.9 \times \exp(-G_{\text{Gaia}}/8.41), & \text{if } G_{\text{Gaia}} < 9, \\ 694.7 \times \exp(-G_{\text{Gaia}}/4.04), & \text{if } G_{\text{Gaia}} \geq 9. \end{cases} \quad (1)$$

Finally, we mask regions affected by stray light, which is caused by light from bright stars or other objects reaching the detector via a non-normal path in the telescope. The same masks are applied for HSC-*i2*, HSC-*z*, and NB872 images in the individual fields. In the following analysis, we exclude the regions outside the FoV of HSC; namely, we use the inner regions of the black circle in Fig. 2. After masking these regions, we measure the effective areas by scattering the random points at a number density of 100 arcmin^{-2} in the non-masked regions. The measured effective areas are 5173 arcmin^2 , 4837 arcmin^2 , 5092 arcmin^2 , and 5137 arcmin^2 for the J0844-0132, J0918+0139, J1425-0015, and J1512+4422 fields, respectively.

We measure the 5σ depth $m_{5\sigma}$ of all filters used in this study in the individual fields, which are summarized in Table 2. In `hscpipe`, the field is divided into small square regions ($\sim 11' \times 11'$), each of which is called a patch. We perform aperture photometry with $1''.5$ diameter apertures at 1,000 random positions, avoiding the masked regions for each patch. We fit a Gaussian to the measured flux histogram and measure the 5σ depth based on its standard deviation. The measured 5σ limiting magnitudes of the individual patches are shown in Fig.

Table 1. Overview of the physical properties of the target quasars and the effective area of our HSC observations for the individual objects. All of the quasar redshifts are the systemic redshifts determined by the [O III] $\lambda 5007$ line (Onoue et al. in prep.).

Field	Effective area (arcmin ²)	R.A. (J2000)	Decl. (J2000)	M_{1450} (mag)	z_{qso}	Discovery paper
J0844–0132	5173	08:44:08.61	–01:32:16.5	–23.97	6.182989 ± 0.000009	Matsuoka et al. (2018b)
J0918+0139	4837	09:18:33.17	+01:39:23.4	–23.71	6.178551 ± 0.000286	Matsuoka et al. (2018b)
J1425–0015	5092	14:25:17.72	–00:15:40.8	–23.44	6.178015 ± 0.000474	Matsuoka et al. (2018a)
J1512+4422	5137	15:12:48.71	+44:22:17.5	–22.07	6.180607 ± 0.000370	Matsuoka et al. (2019b)

Table 2. Summary of the observations except for HSC-SSP and the imaging data in this study. The seeing is the median value of the observations, and the 5σ depth is the median value of the patches.

Field	Filter	Exposure time (hr)	Seeing (‘‘)	$m_{5\sigma}^{\dagger}$ (mag)	Observation date
J0844–0132	HSC- <i>i2</i>	1.11	0.95	26.27	2024 Nov. 26
	HSC- <i>z</i>	1.17	1.31	25.46	2024 Dec. 29, 2024 Dec. 30, 2024 Dec. 31
	NB872	5.25	0.57	25.08	2024 Dec. 21, 2024 Dec. 22, 2024 Dec. 27, 2024 Dec. 28
J0918+0139	HSC- <i>i2</i>	1.11	0.87	26.25	2024 Nov. 26, 2024 Dec. 1
	HSC- <i>z</i>	0.92	1.08	25.55	2024 Dec. 29, 2024 Dec. 30
	NB872	5.25	1.14	25.13	2024 Dec. 28, 2025 Jan. 2
J1425–0015	HSC- <i>i2</i>	1.08	1.23	26.11	2025 Mar. 7
	HSC- <i>z</i>	0 [‡]	N/A	25.00	N/A
	NB872	3.75	0.68	24.75	2025 Apr. 23
J1512+4422	HSC- <i>i2</i>	2.38	1.01	26.76	2025 Feb. 23, 2025 Mar. 7
	HSC- <i>z</i>	0.21	1.26	24.96	2025 Jul. 19
	NB872	7.50	0.90	25.39	2025 Feb. 28, 2025 Mar. 5

[†] The 5σ depth is measured for the final coadd images that are constructed from the data of HSC-SSP and our observations.

[‡] This observation was not performed in our HSC queue observations, so only HSC-SSP data is used.

Table 3. Summary of the applied flags.

Flag	Filter	Value	Comment
<code>detect_isPrimary</code>	i2, z, NB872	True	True if source has no children and is in the inner region of a coadd patch and is in the inner region of a coadd tract and is not detected in a pseudo-filter
<code>base_PixelFlags_flag_bad</code>	i2, z, NB872	False	Bad pixel in the Source footprint
<code>base_PixelFlags_flag_interpolatedCenter</code>	i2, z, NB872	False	Interpolated pixel in the Source footprint
<code>base_PixelFlags_flag_saturatedCenter</code>	i2, z, NB872	False	Saturated pixel in the Source footprint
<code>merge_peak_N872</code>	NB872	True	Peak detected in NB872
<code>base_Blendedness_abs</code>	NB872	< 0.2	Measure of how much the flux is affected by neighbours: $(1 - \text{child_instFlux}/\text{parent_instFlux})$. Operates on the absolute value of the pixels to try to obtain a "de-noised" value.

2. The rms of the limiting magnitudes of the NB872 image in the individual patches within the diameter of HSC is ~ 0.2 mag.

2.2 LAE selection

We model the UV spectrum of LAEs assuming that the continuum ($f_{\lambda, \text{cont}}$) and the Ly α emission ($f_{\lambda, \text{line}}$) can be described by a power-law function and a Gaussian, respectively:

$$f_{\lambda, \text{cont}} \propto \lambda^{\alpha}, \quad (2)$$

$$f_{\lambda, \text{line}} \propto \exp \left[-\frac{(\lambda - \lambda_{\text{Ly}\alpha})^2}{2\sigma_{\lambda}^2} \right], \quad (3)$$

where α is the UV spectral slope per unit wavelength, $\lambda_{\text{Ly}\alpha}$ is the wavelength of the Ly α emission in the observed frame, and σ_{λ} is the standard deviation of the Gaussian. The flux ratio $f_{\lambda, \text{line}}/f_{\lambda, \text{cont}}$ is

determined by the equivalent width (EW_0) of the Ly α emission in the rest frame. The model spectrum of the LAE is defined by summing the continuum and emission line components after the IGM absorption from Madau (1995) is applied. We calculate the colour of an LAE with different redshifts, FWHM and thus σ_{λ} , α , and EW_0 to track it in a colour-colour diagram. We find that the FWHM has little impact on the colour, hence we fix it to 250 km s^{-1} , which is a reasonable FWHM of LAEs at $z \sim 6$ (Prieto-Lyon et al. 2025). Regarding α , we calculate the colour using $\alpha = -3.5, -2.5, -1.5$, which lie within the typical value of LAEs at $z \sim 6$ (Jiang et al. 2013). Fig. 3 shows the colour-colour diagram with the track of the LAE. It should be noted that the FWHM of NB872 corresponds to ~ 22 cMpc, which is larger than the expected overdensity scale (~ 10 cMpc).

Based on this simulation, we use the following criteria to select LAEs at $z \sim 6.18$ with $\text{EW}_0 > 15 \text{ \AA}$ (see the area outlined by black

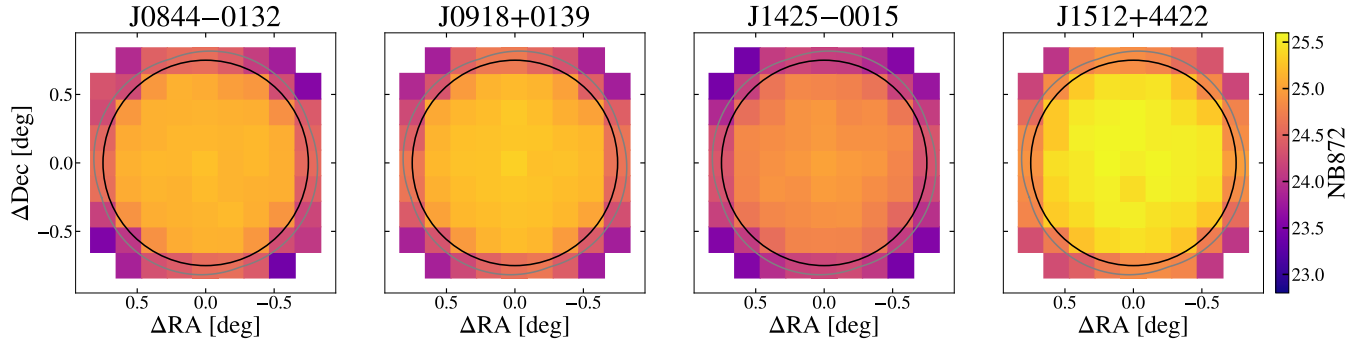


Figure 2. 5σ depth maps of the individual fields. The colour of each patch shows the limiting magnitudes of the NB872 image. The x -axis and y -axis represent the offset from the quasar coordinate. The black solid line displays the diameter of HSC ($45'$). The grey solid line shows the observed field by NB872, taking the dithering into account.

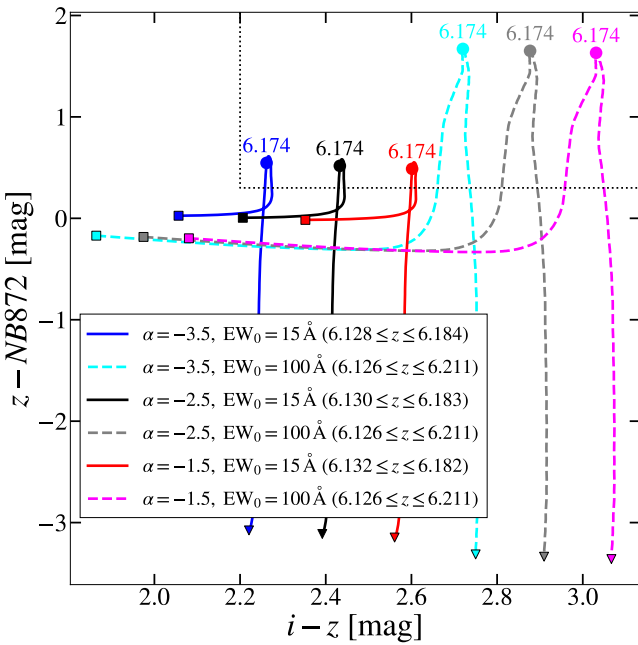


Figure 3. Colour-colour diagram of the simulated spectra. The solid and dashed lines represent the redshift evolution of the simulated spectra from $z = 6$ (squares) to $z = 6.25$ (triangles) with a step of $\Delta z = 0.001$. The legends display the assumed UV continuum slopes, EW_0 , and the redshift range falling within the selection box. The circles show the colour of LAEs at $z = 6.174$, whose Ly α emission lies at the centre of NB872. The dotted lines show the colour criteria to select LAEs with $EW_0 > 15 \text{ \AA}$.

lines in Fig. 3):

$$NB872 < NB872_{5\sigma} \& \quad (4)$$

$$z - NB872 > 0.3 \& \quad (5)$$

$$(i - z > 2.2 \text{ or } i > i_{3\sigma}), \quad (6)$$

where $NB872_{5\sigma}$ is the 5σ depth of the NB872 image, and $i_{3\sigma}$ represents the 3σ depth of HSC- $i2$. If the broadband magnitudes are fainter than 2σ depth, we replace the magnitude with the 2σ depth.

In addition to these criteria, we use the following criterion:

$$\Sigma = \frac{1 - 10^{-0.4(z - NB872)}}{10^{-0.4(ZP_{NB872} - NB872)} \sqrt{\sigma_z^2 + \sigma_{NB872}^2}} > 3, \quad (7)$$

where ZP_{NB872} is the magnitude zeropoint of the NB872 image, and σ_z and σ_{NB872} are the 1σ flux errors of HSC- z and NB872 images, respectively. Σ is the narrowband excess parameter, which quantifies the significance of flux excess of $NB872$ over z , and is used to ensure that the excess in the narrowband is not due to statistical fluctuation (Bunker et al. 1995; Sobral et al. 2013). For selection completeness, defined as the recovery rate of LAEs selected by our colour selection for each specific EW_0 range, see Appendix A. Finally, we perform visual inspection for all of the selected LAE candidates to remove artefacts. In this process, 255, 409, 129, and 126 objects are removed, and 88, 31, 28, and 23 LAEs are finally selected in the J0844-0132, J0918+0139, J1425-0015, and J1512+4422 fields, respectively. We note that we remove the central quasars in all of the fields from these LAEs. Fig. 4 shows the colour-magnitude diagrams with the selected LAEs.

We estimate the detection completeness for each patch in each field using mock observations. We create mock LAEs with Galsim⁴ (Rowe et al. 2015) as a Sérsic profile. Based on the average values of Lyman-break galaxies (LBGs) at $z \sim 6$ (Shibuya et al. 2015), the mock LAEs have the Sérsic index of $n = 1.5$ and the half-light radius of $r_c \sim 0.9$ kpc, which corresponds to $0''.16$ at $z = 6.18$. The magnitudes of the mock LAEs are set in 0.5-magnitude increments from 21.75 mag to 25.75 mag. We embed 100 mock LAEs per patch and magnitude set into NB872 images after convolving the Point Spread Function (PSF) modelled by PSFEx⁵ (Bertin 2011). The redshift of LAEs is fixed at $z = 6.18$. The mock injected images are processed by hscpipe in the same procedure as described in Sec. 2.1, and the completeness is calculated as the recovery rate of the mock LAEs for each patch in each field. The median completeness as a function of a source magnitude for the individual fields is shown in Fig. 5.

⁴ <https://github.com/GalSim-developers/GalSim>

⁵ <https://github.com/astromatic/psfex>

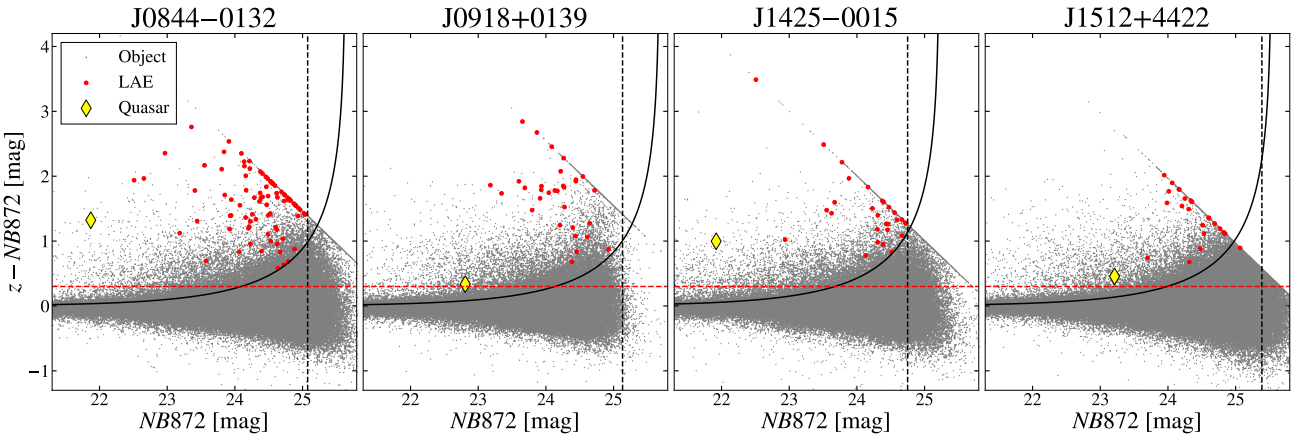


Figure 4. Colour-magnitude diagrams in the individual quasar fields. The grey points show the detected objects. The red points represent the selected LAEs, and the yellow diamonds indicate the quasars' colours. We replace the z -band magnitude with its 2σ limiting magnitude for the objects whose z -band magnitudes are fainter than the 2σ limiting magnitude. This gives the diagonal envelopes on the right of each panel. The red dashed lines denote the narrowband excess threshold of equation (5). The black solid lines represent the narrowband excess parameter of equation (7) with the median 1σ flux errors. The black dashed lines are the 5σ limiting magnitudes of NB872.

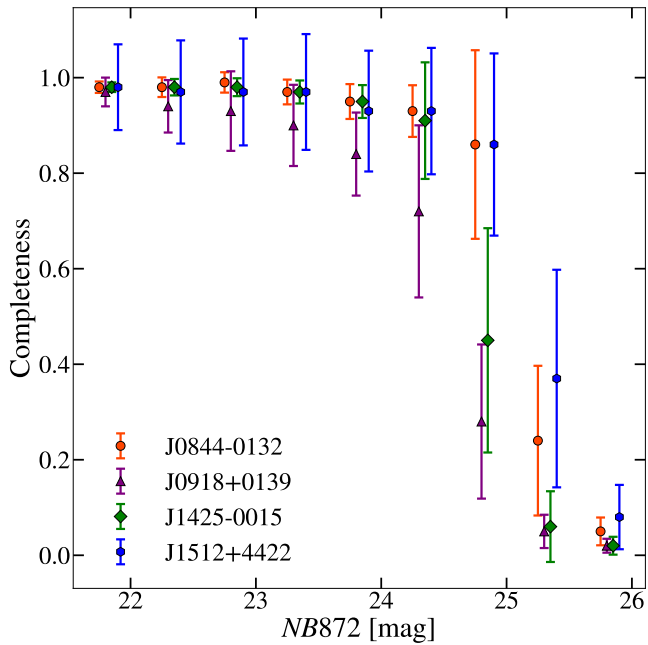


Figure 5. Detection completeness as a function of narrowband magnitudes. We calculate the detection completeness of patches within a FoV of HSC (black circles in Fig. 2). The median detection completeness of the patches and the scatter in the individual quasar fields are plotted. For visibility, the plots for individual fields are slightly offset.

3 RESULTS

3.1 Surface number density of LAEs

We calculate the surface number density of LAEs in the individual fields. Although all of the quasars are selected as LAEs, they are removed in the following analysis. We correct the raw surface number densities by multiplying them by the inverse of the detection completeness in each patch. Fig. 6 shows the surface number density of LAEs in the outskirts of each field, measured at projected distances greater than 50 cMpc ($\sim 20'$ at $z = 6.18$) from the central quasars.

This threshold, also used in a similar study by Wang et al. (2023), is chosen to measure the LAE number density of blank fields around the large proto-clusters known at $z > 6$ (Jiang et al. 2018). Although the threshold will be much larger than the proximity zone size of our quasars, we set the value to evaluate the LAE number density in blank fields. We compare the surface number density of LAEs in the quasar fields with that in blank fields (Konno et al. 2018), which use narrowbands of NB816 ($\lambda_c = 8170 \text{ \AA}$, FWHM = 131 \AA) and NB921 ($\lambda_c = 9210 \text{ \AA}$, FWHM = 120 \AA) on Subaru/HSC to select the LAEs with $\text{EW}_0 > 10 \text{ \AA}$ at $z = 5.7$ and $z = 6.6$ in total areas of 14 and 21 deg^2 in the HSC-SSP Deep/UltraDeep layer, respectively. For a fair comparison, we select LAEs with $\text{EW}_0 > 15 \text{ \AA}$ from the LAEs in Konno et al. (2018) by applying the more stringent colour criteria based on the same model in Sec. 2.2: $i - \text{NB816} > 1.3$ for $z = 5.7$ LAEs; $z - \text{NB921} > 1.2$ for $z = 6.6$ LAEs. We find that the surface number densities of the fields where the effect of the quasar radiation can fully be ignored are almost comparable to those in the blank fields at similar redshifts, but the difference among the quasar fields might be caused by cosmic variance.

3.2 Overdensity of LAEs

We evaluate the overdensity of LAEs using the kernel density estimation (KDE) to calculate the LAE overdensity. We adopt 2D Gaussian kernel $K(X_i, X_0)$:

$$K(X_i, X_0) = \frac{1}{2\pi b^2} \exp \left[-\frac{r(X_i, X_0)^2}{2b^2} \right], \quad (8)$$

where b is the bandwidth, and $r(X_i, X_0)$ is the haversine distance between positions on the sky X_i and X_0 . We apply a cross-correlation length of 17.7 cMpc between galaxies and quasars (Arita et al. 2023) to the bandwidth, yielding $b = 10.5$ at $z = 6.18$, as it denotes the typical clustering scale between them. The galaxy overdensity δ_{LAE} is defined as

$$\delta_{\text{LAE}} = \frac{\Sigma_{\text{LAE}}}{\langle \Sigma_{\text{LAE}} \rangle} - 1, \quad (9)$$

where $\langle \Sigma_{\text{LAE}} \rangle$ is the mean number density of LAEs in the individual fields. We calculate $\langle \Sigma_{\text{LAE}} \rangle$ using the LAEs located > 50 cMpc away

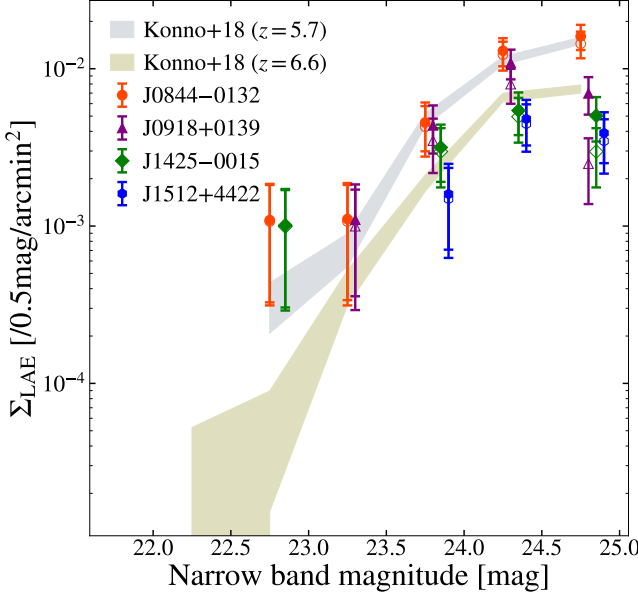


Figure 6. Surface number density of the LAEs with $r > 50$ cMpc in the individual fields, where r is the separation between the LAEs and the central quasars. The open circles show the raw counts, and the filled circles display the completeness-corrected values. The grey and olive shaded regions show the surface number density of LAEs with $EW_0 > 15$ Å in blank fields at $z = 5.7$ and $z = 6.6$ within 1σ error, respectively, as measured by Konno et al. (2018). The data points are slightly offset for visibility.

from the central quasars. $\Sigma_{\text{LAE,obs}}$ is the surface number density of observed LAEs at the position X_i , expressed as

$$\Sigma_{\text{LAE,obs}}(X_i) = \frac{\sum_k w_k K(X_k, X_i)}{\sum_k w_k}, \quad (10)$$

where w_k is the weight of the k th galaxy. We use the inverse of the detection completeness as a function of the narrowband magnitude from Fig. 5 for the weight. Since the sensitivity drops off close to the edge of the HSC FoV, the weight is also used to compute $\langle \Sigma_{\text{LAE}} \rangle$. The error of δ_{LAE} is evaluated by propagating the Poisson statistics of the surface number densities.

To take the spatial bias of sensitivity into account in the overdensity maps, we construct the completeness maps computed in Sec. 2.2. We fit the detection completeness of each patch with the following function of the narrowband magnitude (Serjeant et al. 2000):

$$f(m_{\text{AB}}) = \frac{f_{\text{max}} - f_{\text{min}}}{2} (\tanh[\alpha(m_{\text{AB}}^{50} - m_{\text{AB}})] + 1) + f_{\text{min}}, \quad (11)$$

where f_{max} and f_{min} are the detection completeness at the brightest and faintest magnitude, α quantifies the sharpness of the function, and m_{AB}^{50} is the magnitude where the detection completeness becomes 50%. These parameters are determined based on the χ^2 -fit to the detection completeness of each patch. We calculate the detection completeness from the narrowband magnitudes of LAEs and use the reciprocal of the detection completeness as the weight to account for the spatial variation in the detection completeness. Namely, the weight is expressed as

$$w_k = \frac{1}{f_k(NB872_k)}, \quad (12)$$

where f_k shows the fitted function of the patch containing the k th galaxy, and $NB872_k$ is the narrowband magnitude of the galaxy. After

this correction, the average LAE surface number densities $\langle \Sigma_{\text{LAE}} \rangle$ are 0.009 ± 0.002 , 0.009 ± 0.002 , 0.006 ± 0.001 , and 0.004 ± 0.001 arcmin^{-2} for the four fields. The difference of $\langle \Sigma_{\text{LAE}} \rangle$ among our quasar fields is probably due to the cosmic variance. Using these average values for each of these, we calculate δ_{LAE} of the individual fields.

We also correct the edge effect because the survey area is limited and has several masked regions. The true surface number density is estimated as (Jones 1993)

$$\Sigma_{\text{LAE}}(X_i) = \frac{\Sigma_{\text{LAE,obs}}(X_i)}{\int_S K(X, X_i) dS}, \quad (13)$$

where the integration is computed over the entire survey area without masked regions (S). Fig. 7 shows the resulting LAE overdensity maps. The corrected LAE overdensities at the quasar positions are evaluated as $\delta_{\text{LAE}} = 3.77 \pm 0.97$, 0.01 ± 0.21 , 0.26 ± 0.31 , and 0.13 ± 0.32 in the J0844-0132, J0918+0139, J1425-0015, and J1512+4422 fields, respectively. They are summarized in Table 4. These results show that J0844-0132 resides in an LAE overdense region, while the other quasars do not show any significant overdensity or underdensity.

3.3 EW₀ distribution

We measure EW_0 of our LAEs using the spectrum model described in Sec. 2.2. Assuming that the LAEs have $\alpha = -2.5$, and their Ly α emissions have a FWHM of 250 km s^{-1} at the centre of NB872, we derive the relation between EW_0 and $z - NB872$ colour. In our spectrum model, $z - NB872$ colour converges to ~ 2.0 as EW_0 approaches 240 \AA , the upper limit of the normal star-forming galaxies (SFGs) with $Z > 0.02Z_{\odot}$ (Schaerer 2003). Since our spectrum model does not consider complicated physical situations (e.g. very young galaxies, top-heavy initial mass function), which make Ly α emission stronger than normal galaxies, and faint LAEs have a large uncertainty in z -band magnitudes, we evaluate EW_0 of LAEs with $z - NB872 \gtrsim 2.0$ as a lower limit of 240 \AA . We evaluate the EW_0 error based on the 1σ uncertainty of the $z - NB872$ colour.

Fig. 8 shows the relation between EW_0 of the surrounding LAEs and their separation from the central quasars (θ). We verify the correlation significance by using Kendall's τ and the p -value under the null hypothesis that EW_0 are not correlated with θ . We use `pymccorrelation`⁶ (Curran 2014; Privon et al. 2020), which compute Kendall's τ and the p -value with censored data following Isobe et al. (1986). This hypothesis testing results in $p = 0.433^{+0.396}_{-0.321}$, $0.421^{+0.379}_{-0.315}$, $0.295^{+0.453}_{-0.250}$ and $0.050^{+0.270}_{-0.045}$ for the J0844-0132, J0918+0139, J1425-0015, and J1512+4422 fields, respectively. The errors of the p -values are based on the 1000 times bootstrap resampling. The first three p -values suggest that the null hypothesis cannot be rejected. While the p -value for the J1512+4422 field almost meets $p < 0.05$, its large uncertainty implies that the relation between EW_0 and θ remains merely suggestive. Therefore, we conclude that EW_0 has no clear correlation with θ for all of our quasar fields.

⁶ <https://github.com/privong/pymccorrelation>

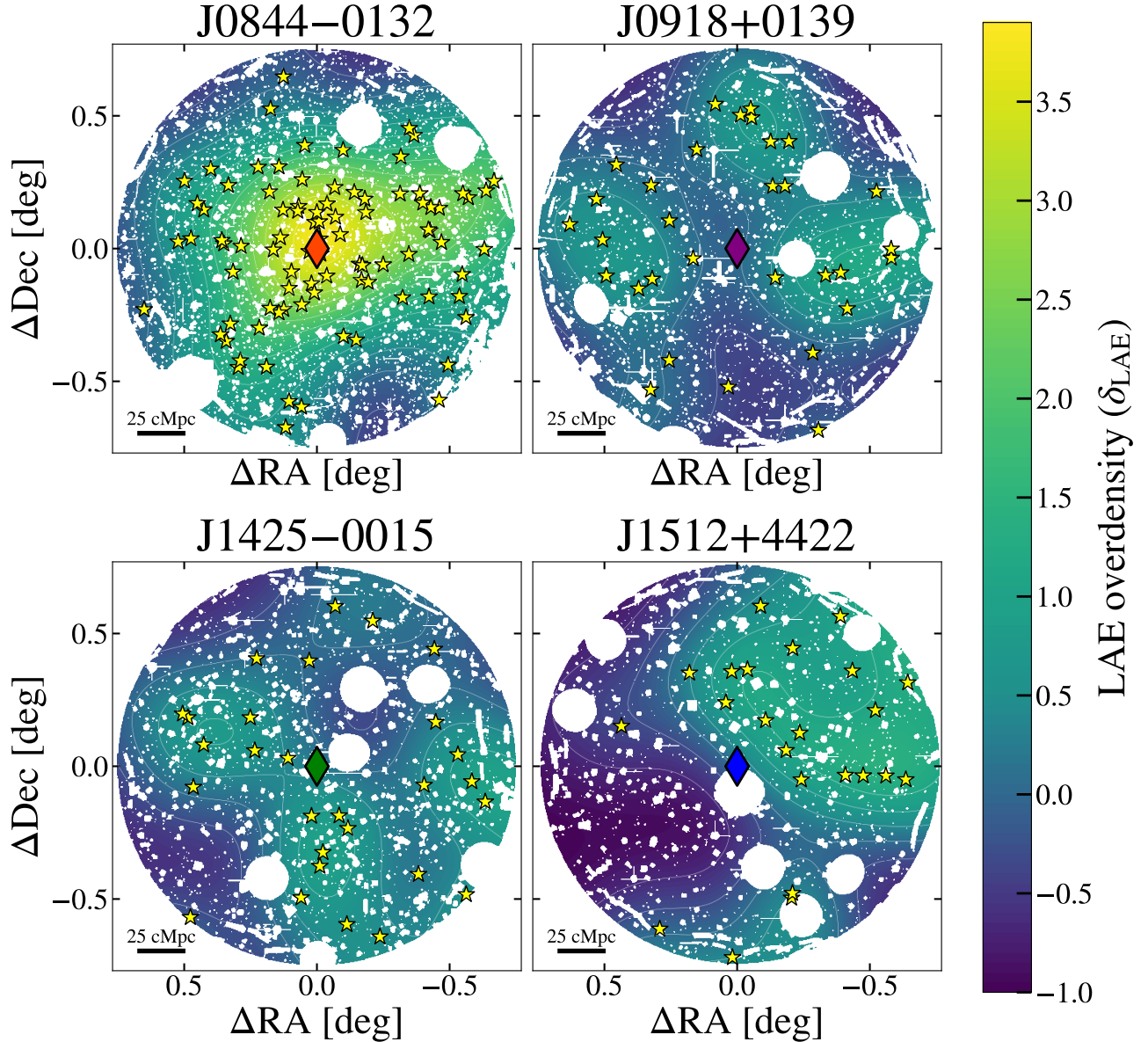


Figure 7. LAE overdensity maps of the individual fields. The abscissa and ordinate represent the offset from the quasar coordinate. The yellow stars and coloured diamonds represent the LAEs and the central quasars, respectively. The underlying colour and contours show δ_{LAE} at each position calculated with equation (9) after applying the detection completeness correction and the edge correction in equations (11) and (13).

4 DISCUSSION

4.1 Photoevaporation effect

4.1.1 Proximity zone size measurement

We measure the proximity zone sizes of our quasars using their FO-CAS spectra⁷. Their spectral coverage is from $0.75 \mu\text{m}$ to $1.05 \mu\text{m}$ with a resolution $R \sim 1200$. First, we infer the intrinsic quasar spectra using an unsupervised probabilistic model named quasar factor analysis (QFA)⁸; Sun et al. (2023). QFA predicts the intrinsic quasar continua based on the latent factor analysis, which is a statis-

tical framework that assumes that a high-dimensional correlated data (the quasar continua) set can be expressed as linear combinations of a small set of lower-dimensional latent factors (e.g. Ly α emission, power-law feature of quasar continua, C IV emission), combined with the physical priors of the IGM. Sun et al. (2023) demonstrate that QFA achieves lower absolute fractional flux error in the recovered quasar continua than the conventional principal component analysis-based method. QFA uses the quasar spectra normalized by the flux at 1280 \AA in the rest frame, the flux uncertainty, and the systemic redshift determined by [O III] $\lambda 5007$ emission in Table 1. When applying QFA to our quasars' spectra, we conform the observed spectra onto a uniform rest-frame wavelength grid from 1030 \AA to 1600 \AA with a logarithmic uniform spacing (median pixel size is $\sim 0.3 \text{ \AA}$, corresponding to $\sim 0.014 \text{ pMpc}$) and mask some wavelength ranges where the normalized flux shows low signal-to-noise ratios. The

⁷ The spectra of our quasars are published on <https://cosmos.phys.sci.ehime-u.ac.jp/~yk.matsuoka/shellqs.html>.

⁸ <https://github.com/ZechangSun/QFA>

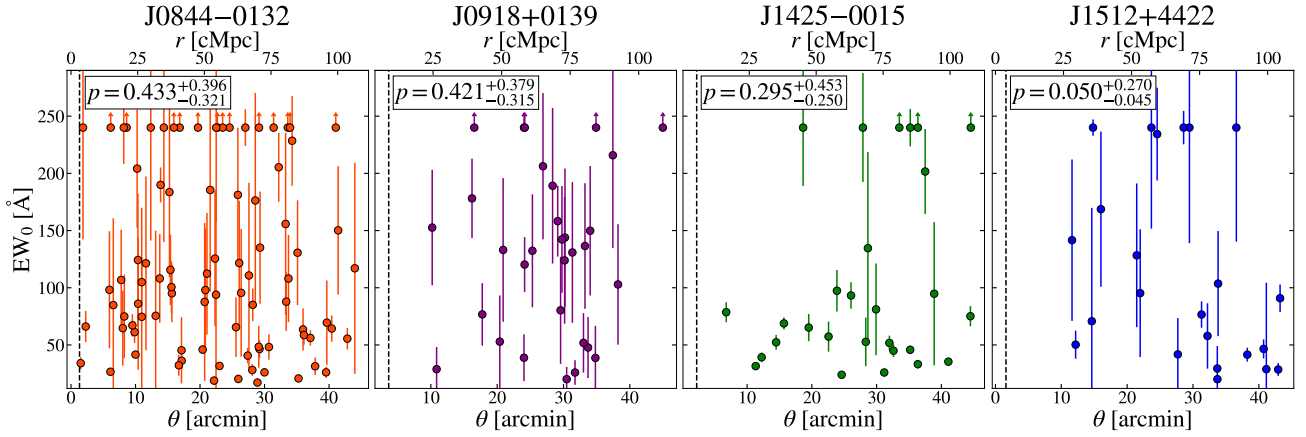


Figure 8. Relation between EW_0 and the separation between the LAEs and the central quasars (θ) of the individual quasar fields. The vertical dashed lines show the proximity zone sizes described in Sec. 4.1.1. We note that no LAEs reside within the proximity zone of the quasars. The left top of each panel shows the p -value.

QFA-predicted quasar continua are shown in Fig. 9 with the observed quasar spectra.

We measure the proximity zone size following the standard definition used in the literature (e.g. Fan et al. 2006; Carilli et al. 2010; Venemans et al. 2015; Eilers et al. 2017; Ishimoto et al. 2020). We smooth the quasar spectra with a 20 Å wide (observed frame) boxcar function. The smoothing scale corresponds to 0.93 pMpc at $z = 6.18$. The IGM transmission is computed as the ratio of the smoothed quasar spectra and the smoothed QFA-predicted continua. The proximity zone size is defined as the distance to the first of three sequential pixels that show transmission below 10% blueward of the Ly α emission line. The error of the proximity zone size is estimated based on the observed error in the quasar spectra. After randomly adding pixel-to-pixel errors to the quasar spectra, we repeat the measurements of the proximity zone size 1000 times, and consider the variation in these measurements as the error of the proximity zone size. We obtain $R_p = 0.4449 \pm 0.0093$, 1.230 ± 0.156 , 0.7478 ± 0.0404 , 0.5387 ± 0.0373 pMpc for J0844-0132, J0918+0139, J1425-0015, J1512+4422, respectively. For a fair comparison later, we also compute the magnitude-corrected proximity zone size based on M_{1450} following Ishimoto et al. (2020), which is applicable to low-luminosity regimes such as our sample:

$$R_{p,\text{corr}}^{-25} = R_p \times 10^{0.4 \times (M_{1450} + 25) / 1.80}. \quad (14)$$

The corrected proximity zone sizes are $R_{p,\text{corr}}^{-25} = 0.7536 \pm 0.0157$, 2.379 ± 0.302 , 1.661 ± 0.090 , 2.412 ± 0.167 pMpc for J0844-0132, J0918+0139, J1425-0015, J1512+4422, respectively. These results are summarized in Table 4. Fig. 10 shows the IGM transmission based on the quasar continua recovered by QFA.

4.1.2 Does photoevaporation affect LAE overdensity?

We find that no LAEs reside in the proximity zones in all of our quasar fields, as shown in Fig. 8. Despite being an overdense region of LAEs, the J0844-0132 field contains no LAEs within its proximity zone. Applying the δ_{LAE} measured within a 17.7 cMpc radius region around the quasar to the area within the proximity zone yields an expected LAE detection of 0.12. Hence, we cannot conclude that the photoevaporation effect hinders the LAE formation. On the other hand, although the proximity zone size of our quasars is quite small compared to the expected overdensity scale, LAE overdensities are

not observed in the remaining three fields either. This allows us to conclude that, at least in these three regions, the absence of LAE overdensity is not due to photoevaporation effects from the quasars. In estimating the proximity zone size above, it is assumed that quasar radiation is isotropic. We caution that the result may not hold if the quasar radiation is beamed in a specific direction; therefore, spectroscopic confirmation of the LAEs is necessary to verify this possibility. The proximity zone size also depends on the quasars' age, which will be discussed later. Uchiyama et al. (2019) and Suzuki et al. (2025) suggest that LAEs with high Ly α EW_0 are particularly scarce around quasars, as these LAEs are typically low-mass galaxies vulnerable to the photoevaporation effect. However, in our four quasar fields, no statistically significant correlation between EW_0 and θ is concluded as shown in Fig. 8. Our results, which show a broad environment from $\delta_{\text{LAE}} = 0.01$ to $\delta_{\text{LAE}} = 3.77$, indicate that the LAE density around the quasar exhibits diversity independent of the photoevaporation effect.

The absence of LAEs within the proximity zone is also observed in the bright quasar VIK J2348-3054 at $z = 6.90$ (Lambert et al. 2024), located within an LAE overdensity over several pMpc. Lambert et al. (2024) suggest that the absence is caused by the photoevaporation effect, intense quasar radiation that prohibits star formation in its vicinity. On the other hand, several LAEs are found in the proximity zones of the quasars (e.g. Bosman et al. 2020; Protušová et al. 2025). The presence of these LAEs is thought to be due to the effect of locally small H i fractions caused by ionizing photons from quasars rather than photoevaporation.

Quasars with a very small proximity zone size ($R_{p,\text{corr}}^{-25} \lesssim 0.90$ pMpc) are suggested to be very young ($\lesssim 10^4$ yr) (Eilers et al. 2017; Ishimoto et al. 2020). Since it takes time for the IGM to reach ionization equilibrium, the small proximity zone size indicates that the duration of the quasar activity is relatively small, which is confirmed by a radiative transfer simulation by Davies et al. (2020). They solve the time-dependent equations for ionized H and He to compute the effect of the quasar ionizing radiation on the IGM and simulate the Ly α transmission spectrum of quasars with different physical properties (z , M_{1450} , age). Interestingly, only J0844-0132, which resides in an overdense region, meets the criterion of a young ($\lesssim 10^4$ yr) quasar among our quasars. The proximity zone sizes of the remaining three quasars are consistent with the relation between R_p and M_{1450} derived in Ishimoto et al. (2020) within 2σ error, which

Table 4. Physical properties of host galaxies and the SMBHs. The M_* are from Ding et al. (2023, 2025), the SFRs are from Phillips et al. (2025), and the SMBH masses and the bolometric luminosities are from Onoue et al. in prep. We note that the SMBH masses are based on the H β emission lines.

Field	$\langle \Sigma_{\text{LAE}} \rangle$ (arcmin $^{-2}$)	δ_{LAE}	R_p (arcmin)	R_p (pMpc)	R_p^{-25} (pMpc)
J0844–0132	0.009 ± 0.002	3.77 ± 0.97	1.320 ± 0.027	0.4449 ± 0.0093	0.7536 ± 0.0157
J0918+0139	0.009 ± 0.002	0.01 ± 0.21	3.646 ± 0.462	1.230 ± 0.156	2.379 ± 0.302
J1425–0015	0.006 ± 0.001	0.26 ± 0.31	2.218 ± 0.120	0.7478 ± 0.0404	1.661 ± 0.090
J1512+4422	0.004 ± 0.001	0.13 ± 0.32	1.598 ± 0.111	0.5387 ± 0.0373	2.412 ± 0.167
Stellar mass $\log(M_*/M_\odot)$	SFR $(M_\odot \text{ yr}^{-1})$	sSFR (Gyr^{-1})	SMBH mass $\log(M_{\text{BH}}/M_\odot)$		Bolometric luminosity $\log(L_{\text{bol}}/\text{erg s}^{-1})$
$10.03^{+0.53}_{-0.45}$	39^{+9}_{-24}	4^{+9}_{-5}	8.57^{\dagger}		$46.427 \pm 0.001^{\dagger}$
$10.21^{+0.52}_{-0.37}$	—	—	8.57		45.827 ± 0.003
$10.54^{+0.36}_{-0.37}$	37^{+5}_{-27}	$0.8^{+1.2}_{-0.6}$	8.43		45.976 ± 0.003
$10.57^{+0.29}_{-0.41}$	33^{+4}_{-16}	$0.7^{+1.2}_{-0.4}$	9.17		45.728 ± 0.002

[†] Onoue et al. in prep. present the SMBH mass and the bolometric luminosity without the correction for dust extinction, although Matsuoka et al. (2025) show that J0844–0132 is a dust-obscured quasar with $A_V \sim 2$ based on the Balmer decrement. Matsuoka et al. (2025) present the SMBH mass and bolometric luminosity corrected for dust extinction as $\log(M_{\text{BH}}/M_\odot) = 9.11 \pm 0.01$ and $\log(L_{\text{bol}}/\text{erg s}^{-1}) = 47.08 \pm 0.01$.

implies that these quasars are not extraordinarily young. These results suggest that the quasar age could be related to the LAE overdensity in the quasar fields. One interpretation of this relation could be that as long as the quasar is young, its intense radiation would not have had sufficient time even to suppress nearby galaxies > 1 pMpc away from the quasar even if the quasar has sufficiently luminous to hinder their star formation by the photoevaporation effect. However, the current data is too limited to draw strong conclusions, and the scenario needs to be verified with a larger sample.

Moreover, J0844–0132 has both a broad and a narrow component in its H α emission, and a red NIRcam colour comparable to $F356W - F444W > 0.44$ (Matsuoka et al. 2025), which satisfy the rest-optical criteria of the red continuum slope ($\beta_{\text{opt}} > 0$; Kocevski et al. 2025) for Little Red Dots (LRDs⁹). Based on the scenario that LRDs represent the first AGN events associated with newly formed seed BHs (Inayoshi 2025), the quasar may be in the initial phase of the AGN activity that could evolve into UV-luminous quasars (Arita et al. 2025; Schindler et al. 2025), which also supports that J0844–0132 is a young quasar. However, J0844–0132 is a mildly obscured quasar (Matsuoka et al. 2025), and in this case, the number of ionizing photons escaping from the quasar decreases, resulting in a smaller apparent proximity zone size. Consequently, the quasar age estimated from this measurement may be underestimated. It also should be noted that foreground H 1 clouds, such as damped Ly α systems and Lyman Limit systems, may affect the proximity zone size measurements. To determine if this is an effect, deeper spectroscopic follow-up observations are necessary.

4.2 Relation between LAE overdensity and the properties of the host galaxy and SMBH

We discuss whether the physical properties of the quasars are related to the LAE overdensity in their fields. In order to investigate the relation between the various quasar properties and the LAE overdensity, we include seven luminous quasars at $5.7 < z < 7$ from previous studies in Table 5 in addition to our low-luminosity quasars. The effective area of the previous studies listed in Table 5 varies from VLT/MUSE

⁹ The large-scale environments of LRDs are under debate. Some studies suggest that LRDs are formed in an overdense region (e.g. Schindler et al. 2025), others show that LRDs tend to be detected in isolated regions (e.g. Carranza-Escudero et al. 2025).

(~ 1 arcmin 2) to DECam (~ 3 deg 2), depending on the FoV of the instrument used. Four of the luminous quasars (J1030+0524, J0836+0054, J0910–0414, J2348–3054) are in LAE overdense regions, while three (J0203+0012, J2329–0301, J0305–3150) are in non-overdense regions.

4.2.1 Host galaxy properties

Since M_* and DMH mass are positively correlated (Behroozi et al. 2013, 2019), one might expect that quasars hosted by galaxies with high M_* will be found in a galaxy overdense region. The host galaxies of our quasars have been directly detected by JWST, and their M_* and SFR have been measured, which allows us to verify the scenario. We examine the correlation between the LAE overdensity and these host galaxy properties, which are summarized in Table 4. The 10 Myr-scale SFR of J1512+4422 is estimated by Onoue et al. (2025) and Phillips et al. (2025), but the latter estimates a ~ 1 dex higher value than the former. To infer its SFR, the former performs the spectrum energy distribution (SED) fitting to its quasar-decomposed spectrum, while the latter uses the extended H α emission based on the assumption that it is from the star formation activity in the host galaxy. For consistency of the SFR estimate in our quasars, we adopt the SFR by Phillips et al. (2025) for all of our quasars in the following discussion. We note that adopting the SFR for J1512+4422 in Onoue et al. (2025) does not have an impact on the results that the SFRs are not strongly correlated to the LAE overdensity. Another luminous quasar, J1030+0524, known to reside within the LAE high-density region (Mignoli et al. 2020), has had its upper limit of the M_* constrained by the NIRCam imaging with F115W, F200W, and F356W (Yue et al. 2024) as $\log(M_*/M_\odot) < 10.65$ and its SFR derived from the far-infrared (FIR) luminosity measured by ALMA observations (Decarli et al. 2018) as $67 M_\odot \text{ yr}^{-1}$. Due to the extreme brightness of J1030+0524, its host galaxy is not detected in all the PSF-subtracted images, which only allows them to constrain the upper limit of the M_* . We caution that the SFR estimated by FIR luminosity shows the average star formation activity over 100 Myr, which is different from the timescale of H α -based SFR (Kennicutt & Evans 2012). We note that this is the only quasar whose host properties have been measured in Table 5, which summarizes the previous studies on the LAE overdensity around quasars at $6 \lesssim z \lesssim 7$. The LAE overdensity measurement can vary with the limiting magnitude of the sample and the measured spatial range, making quantitative comparisons with past studies difficult. Therefore, we will not consider the significance of

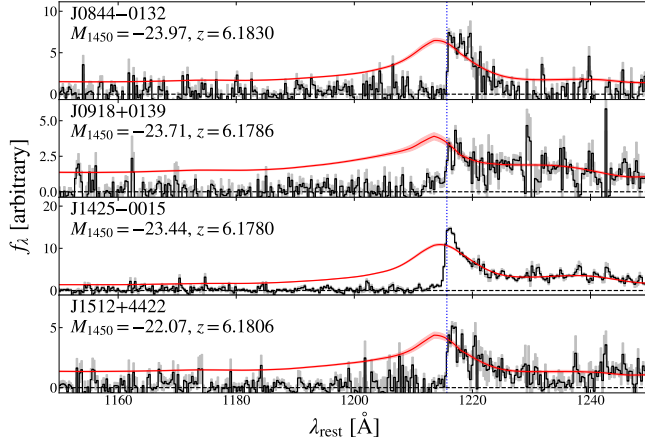


Figure 9. Observed quasar spectra and the quasar continua predicted by QFA. The black lines with the grey shade show the observed quasar spectra with their errors normalized by the flux at 1280 Å in the rest frame. The red lines and shade represent the QFA-predicted quasar continua and their uncertainty. The blue dotted lines indicate the quasar redshift.

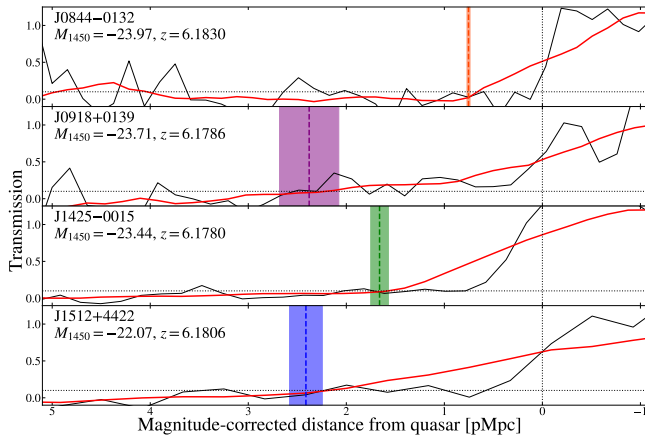


Figure 10. IGM transmission as a function of the magnitude-corrected distance using equation(14) from our quasars. The black lines show the IGM transmission based on the continuum recovered by QFA. The red lines represent the IGM transmission smoothed with a 20 Å wide boxcar function. The horizontal dotted lines show a transmission level of 10%. The vertical dotted lines denote the systemic redshift of the quasars. The dashed lines with the shaded regions show $R_{p,\text{corr}}^{-25}$ and its error.

overdensity here, but only compare whether overdensity is present or not. Fig. 11 shows the relation between the LAE overdensity and the M_* , SFR, specific SFR (sSFR) of the host galaxies. We find that J0844-0132, which exhibits LAE overdensity in our quasars, shows the smallest M_* and the largest sSFR among our quasars, though the differences are smaller than their uncertainties. All of the host galaxies with their SFR available in our quasars are almost along the star-forming main sequence at $z \sim 6$ (Clarke et al. 2024) within the error. We conclude that LAE overdensity does not show clear correlations with the host galaxy properties. For reference, Fig. B1 shows the relationship between host galaxy properties and surrounding overdensity, including results from galaxy populations other than LAEs. In this case, one must be very careful as the galaxies used to measure overdensity, the effective area over which they are measured,

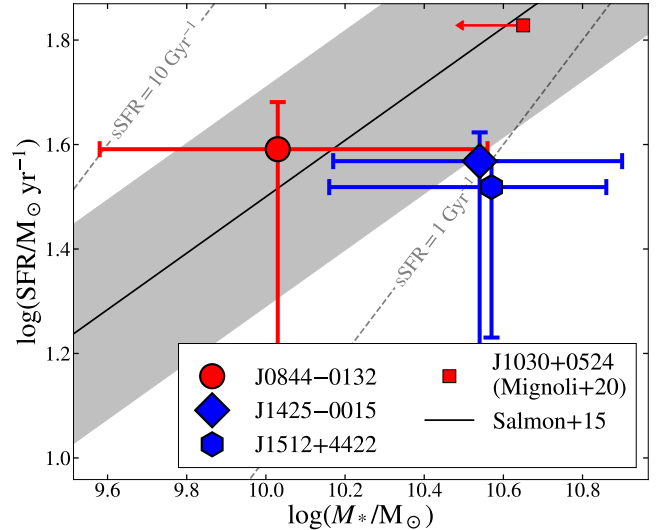


Figure 11. The relationship between M_* and the SFR of the quasars in this study and previous research. The red and blue symbols show that the quasars reside in the LAE overdense and non-overdense regions, respectively. The dashed lines represent $\text{sSFR} = 10 \text{ Gyr}^{-1}$ (top) and $\text{sSFR} = 1 \text{ Gyr}^{-1}$ (bottom). The solid line with the grey shade shows the star-formation main sequence with its uncertainty at $z \sim 6$ (Salmon et al. 2015). The M_* of our quasars are from Ding et al. (2023, 2025), and the SFRs and sSFRs are from Phillips et al. (2025). They do not measure the SFR and sSFR of J0918-0139 because they do not detect its spatially extended H α emission. The M_* and SFR of J1030+0524 are from Yue et al. (2024) and Decarli et al. (2018), and Mignoli et al. (2020) confirm that the quasar resides in an LAE overdense region. Due to the extreme brightness of J1030+0524, they do not detect its host galaxy in all the PSF-subtracted images, so they only constrain the upper limit of the M_* . The SFR is derived from the FIR luminosity following Kennicutt & Evans (2012).

and the methods used to measure SFR and M_* differ. However, no clear correlation is observed.

Contrary to the prediction based on the correlation between M_* and DMH mass, our results showed no such tendency. Ding et al. (2025) show that the host galaxies of our quasars have high M_* , almost massive end of the stellar mass function at $z \sim 6$, but only J0844-0132 resides in an LAE overdense field. This may be because there is a large dispersion in the stellar-to-halo mass ratio of the high- z quasars in addition to the narrow dynamic range of M_* of this sample. Further observations are necessary to investigate the relation between the LAE overdensity and the host M_* .

4.2.2 SMBH properties

We also compare the LAE overdensity of our quasars with their SMBH properties (Onoue et al. in prep.). Fig. 12 shows the comparison of SMBH mass and the bolometric luminosity among quasars, whose LAE overdensity has been examined. We note that Matsuoka et al. (2025) present SMBH mass and bolometric luminosity of J0844-0132 ~ 0.6 dex higher than those from Onoue et al. in prep. by applying the correction for dust extinction. However, while the dust extinction is expected to be $A_V > 10$, the observed Ly α luminosity is highly prominent, leaving uncertainty in this extinction correction. Hence, we adopt these SMBH properties without the correction. The following discussion is not affected by which values are applied. No SMBH parameters appear to be related to the LAE overdensity in

Fig. 12. These results suggest that the SMBH properties are not significantly related to their large-scale environment. This is consistent with the recent results for low-luminosity AGNs at $3.9 < z < 6$ (Lin et al. 2025), which investigate the large-scale environments of 28 low-luminosity AGNs using 782 HAEs to find no clear correlation between the surrounding HAE overdensity and the AGN properties (broad-line luminosity, BH mass, AGN fraction). For reference, Fig. B2 shows the relationship between SMBH properties and surrounding overdensity, including recent results from EIGER and ASPIRE. One must be very careful since the galaxy population used to measure overdensity, and the effective area over which they are measured differ, but no clear correlation is observed.

On the other hand, theoretical studies suggest a correlation between the galaxy overdensity and the SMBH properties. Pizzati et al. (2024) predicts that more luminous quasars appear in more massive DMHs at $z \sim 6$ by combining a large cosmological simulation and observed luminosity function and correlation function of the quasars, although the scatter of the relation is as large as ~ 0.64 dex, the relation could be naturally explained by the scenario that the massive DMH can accumulate a large amount of gas accreting onto the SMBH. This implies that luminous quasars are expected to be observed in galaxy overdense regions. In addition to the bolometric luminosity, Habouzit et al. (2019) show the relation between the galaxy overdensity and the SMBH mass at high- z . They employ the large-scale simulations of Horizon-AGN (Dubois et al. 2014) and Horizon-noAGN (Peirani et al. 2017) to show that SMBHs with $M_{\text{BH}} \geq 10^8 M_{\odot}$ at $z \sim 6$ are embedded in more overdense regions than the galaxy with the same M_* without SMBHs, whose overdensity is statistically significant within 10 cMpc scale, and that the number of surrounding galaxies increases with the SMBH mass. While our targets are limited to four quasars, our results are not consistent with these theoretical predictions. One of the explanations for the inconsistency might be the projection effect. While the three-dimensional distance among galaxies is available in the cosmological simulation, the narrowband observation only provides the projected distance among LAEs, which can dilute the overdensity significance due to the contamination by field galaxies. In fact, the FWHM of NB872 corresponds to 22 cMpc in the line-of-sight distance, which is larger than the expected overdensity scale of ~ 10 cMpc (Habouzit et al. 2019). In order to understand the discrepancy between observations and simulations, follow-up spectroscopy to determine the accurate redshifts of galaxies in the quasar fields is important. Moreover, the large scatter in the relationship between the SMBH and DMH masses due to their indirect connection through the host galaxy can cause the discrepancy. The large scatter also appears in the simulation as Habouzit et al. (2019) reported that some SMBHs show much higher DMH mass than expected from the average black hole mass to DMH mass ratio. Individual DMH mass measurements of quasars (e.g. Fei et al. 2025) also help investigate the relationship between the galaxy overdensity of quasars and their SMBH properties.

4.2.3 Galaxy age

In Sec. 4.2.1 and 4.2.2, we assume that LAEs trace the underlying mass distribution. However, different galaxy populations may show different distributions. In general, galaxies in overdense regions are thought to form earlier and be older than their field counterparts, undergoing accelerated growth in their evolution (e.g. Hatch et al. 2011; Koyama et al. 2013; Cooke et al. 2014). However, stacking analysis of LAEs at $z \sim 6$ -7 shows that they are typically young star-forming galaxies (~ 1 -3 Myr; Ono et al. 2010). Therefore, when discussing the overdense region of LAEs, one may need to be cautious

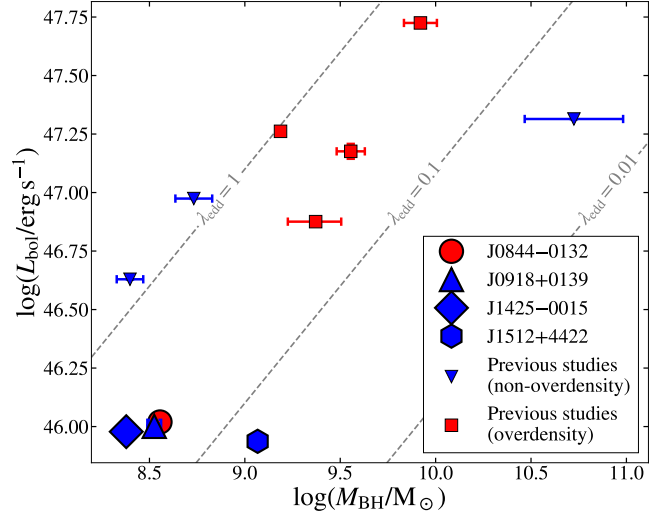


Figure 12. The SMBH masses and the bolometric luminosities of the quasars in this study and literature. The red and blue symbols show the quasars that reside in regions overdense and non-overdense in LAEs, respectively. The dashed lines show the Eddington ratio, $\lambda_{\text{Edd}} = 1, 0.1, 0.01$ from top to bottom. These SMBH properties of our quasars are from Onoue et al. in prep., which estimate the SMBH mass based on the $\text{H}\beta$ emission (Kaspi et al. 2000). We also plot results of the quasars in Table 5 from the literature. We use those parameters in Shen et al. (2019) for J0203+0012 and J0836+0054, Willott et al. (2010) for J2329-0301, Farina et al. (2022) for J0305-3150 and J2348-3054, Yang et al. (2021) for J0910-0414, and Yue et al. (2024) for J1030+0524. Shen et al. (2019) estimate the SMBH mass based on the $\text{C}\text{IV} \lambda 1549$ line (Vestergaard & Peterson 2006) and compute the bolometric luminosity based on the continuum luminosity at 3000 Å in rest-frame with a bolometric correction of 5.15 (Richards et al. 2006). Willott et al. (2010) estimate the SMBH mass based on the $\text{Mg II} \lambda 2798$ line (Vestergaard & Osmer 2009) and compute the bolometric luminosity based on the continuum luminosity at 3000 Å in rest-frame with a bolometric correction of 6 (Richards et al. 2006; Jiang et al. 2006). Farina et al. (2022) and Yang et al. (2021) estimate the SMBH mass based on the $\text{Mg II} \lambda 2798$ line (Vestergaard & Osmer 2009) and the bolometric luminosity from the continuum luminosity at 3000 Å in rest-frame with a bolometric correction of 5.15 (Richards et al. 2006). Yue et al. (2024) estimate the SMBH mass based on the $\text{H}\beta$ line (Vestergaard & Peterson 2006) and the bolometric luminosity from the continuum luminosity at 5100 Å in rest-frame with a bolometric correction of 9.26 (Runnoe et al. 2012). We caution that we use the available SMBH mass measurements in the literature, which induce the SMBH mass measured by different methods.

about the LAEs' young age. In fact, at lower- z ($2 < z < 4.5$), Ito et al. (2021) point out that the cross-correlation between LAEs and SFGs is lower than SFGs' auto-correlations, and that LAEs are less abundant in SFG overdense regions. This suggests that LAEs may exhibit a formation epoch-dependent assembly bias and that they tend to be observed away from old populations.

Among our quasars, the spectrum of the host galaxy of J1512+4422 obtained by JWST shows characteristics of a post-starburst galaxy (Onoue et al. 2025), and its mass-weighted age is 150^{+20}_{-20} Myr, which is much older than the typical LAE age. Therefore, even if there is no LAE overdensity in the J1512+4422 field, it cannot be ruled out that galaxies too old to be observed as LAEs are clustering there. It is intriguing to measure the overdensity of the galaxy population other than LAEs in this field, as well as in J0918+0139 and J1425-0015 fields, where LAE underdensity is observed, possibly resulting in similar situations. It can be inferred that the number density of young galaxies (e.g. HAEs) is relatively

Table 5. Previous studies on the LAE overdensity over Mpc-scale around luminous quasars at $5.7 < z < 7$. The effective area in this table represents the area to search for LAEs homogeneously.

Quasar	z	M_{1450} (mag)	Effective area (arcmin 2)	Overdensity	Redshift ref.	Overdensity ref.	Comments
ULAS J020332.38+001229.2	5.72	-26.2	44	No	(1)	(8)	
PSO J215.1512–16.0417	5.73	-27.6	37	No	(2)	(9)	No M_{BH} measurement
SDSS J083643.85+005453.3	5.81	-27.8	11	Yes	(3)	(10)	
SDSS J103027.10+052455.0	6.31	-27.1	1	Yes [‡]	(4)	(11)	M_* and SFR have been measured in Yue et al. (2024) and Decarli et al. (2018) , respectively.
CFHQS J232908–030158.8	6.42	-25.2	788	No [†]	(5)	(12)	
VIKING J030516.92–315056.0	6.61	-26.0	697	No	(6)	(13)	
DELS J091054.53–041406.8	6.63	-26.4	3740	Yes	(7)	(14)	
VIKING J234833.34–305410.0	6.90	-25.7	10332	Yes	(4)	(15)	

References: (1) [Venemans et al. \(2007\)](#); (2) [Bañados et al. \(2014\)](#); (3) [Bañados et al. \(2016\)](#); (4) [Kurk et al. \(2007\)](#); (5) [Willott et al. \(2007\)](#); (6) [Venemans et al. \(2013\)](#); (7) [Wang et al. \(2019b\)](#); (8) [Bañados et al. \(2013\)](#); (9) [Mazzucchelli et al. \(2017\)](#); (10) [Overzier \(2022\)](#); (11) [Mignoli et al. \(2020\)](#); (12) [Goto et al. \(2017\)](#); (13) [Ota et al. \(2018\)](#); (14) [Wang et al. \(2024\)](#); (15) [Lambert et al. \(2024\)](#)

[†] [Farina et al. \(2017\)](#) discovered an LAE by VLT/MUSE at ~ 12.5 pkpc and 560 km s^{-1} from CFHQS J232908–030158.8, suggesting that the quasar resides in the high-density environment. However, the FoV of MUSE is much smaller than that of Subaru/Suprime-Cam used in [Goto et al. \(2017\)](#). This study focuses on the LAE distribution in the high- z quasar fields with a large FoV, so we include CFHQS J232908–030158.8 in the quasars not residing in an LAE overdense field.

[‡] [Balmaverde et al. \(2017\)](#) presented 21 robust LBGs in this quasar field ($\sim 25' \times 25'$) using multiband photometry of Y, J -bands from WIRCam on Canada-France-Hawaii Telescope and literature (r, i, z -bands: [Morselli et al. 2014](#); H, K -bands: [Quadri et al. 2007](#); [Blanc et al. 2008](#); Spitzer Infrared Array Camera 3.4 and $4.5 \mu\text{m}$ bands: Spitzer Heritage Archive), and [Mignoli et al. \(2020\)](#) performed spectroscopic follow-up observations for 12 objects to find that nine of them are real galaxies at $z > 5.7$. They reported that four galaxies are associated with the large-scale structure of SDSS J010013.02+280225.8 and that three of them show $\text{EW}_0 > 15 \text{ \AA}$, which can be regarded as LAEs. Therefore, while we treat CFHQS J232908–030158.8 as a quasar in a non-overdense region, we count SDSS J103027.10+052455.0 among quasars in overdense regions.

small, while that of quiescent galaxies as old as the host galaxy of J1512+4422 is higher than that in blank fields.

4.3 LAE overdensity around galaxies with a similar M_* as our quasars

Our quasar samples leverage the advantage of known host galaxy M_* , allowing us to discuss the impact of AGN occurrence on LAE overdensity by comparing it to the LAE overdensity surrounding non-AGN galaxies with the same M_* .

4.3.1 LAE and galaxy data

Ideally, we would select LAEs around galaxies under conditions identical to those described in Sec. 3.2. However, since no large LAE sample exists at our quasars’ redshifts, we substitute a sample of LAEs at $5.65 \leq z \leq 5.75$, which is close to this redshift, and LAE evolution during this interval ($\Delta z \sim 0.48$ corresponds to ~ 0.1 Gyr) is likely to be small. [Santos et al. \(2016\)](#) present photometrically selected LAEs at $z \sim 5.7$ in the survey area of 7 deg^2 in the following three survey fields: the Cosmic Evolution Survey (COSMOS; [Scoville et al. 2007](#)) field, the UKIDSS Ultra Deep Survey (UDS; [Lawrence et al. 2007](#)) field, and the SA22 field. The effective area of the COSMOS field is 1.96 deg^2 (7056 arcmin^2). They use multiband photometry ($BVgriJK$) in addition to NB816 and perform careful visual inspection to remove low- z interlopers. We use the LAEs in the COSMOS field out of those in the three fields. As discussed later, the COSMOS field has abundant multi-wavelength data, allowing M_* estimates for each galaxy via SED fitting. They select LAEs with $\text{EW}_0 > 25 \text{ \AA}$ from narrowband imaging, while our LAE sample is selected with $\text{EW}_0 > 15 \text{ \AA}$. For a fair comparison, we reevaluate the LAE overdensity of our quasar fields using the LAEs with $\text{EW}_0 > 25 \text{ \AA}$, which can be selected by $z - \text{NB872} > 0.9$ based on the simulation described in Sec. 2.2.

We select spectroscopically confirmed galaxies with M_* equivalent to those of our quasars from COSMOS Spectroscopic Redshift Compilation¹⁰ ([Khstovyan et al. 2026](#)). The M_* is evaluated by the SED fitting with CIGALE¹¹ ([Boquien et al. 2019](#); [Yang et al. 2020a](#)); for details on the parameters, please refer to [Khstovyan et al. \(2026\)](#). There are 18 galaxies with $9.5 \leq \log(M_*/\text{M}_\odot) \leq 11.5$ at $5.65 \leq z \leq 5.75$, the same redshift range as the LAEs. Taking the goodness-of-fit of the SED fitting and the reliability of the spectroscopic redshift, we select 5 galaxies that satisfy $\chi_\nu^2 < 5$ and $3 \leq Q_f < 9$ out of the 18 galaxies. Here, Q_f indicates the quality flag, and this criterion selects galaxies whose redshift confidence level is $\geq 95\%$ and emission lines do not have broad line components. In the case of $Q_f \geq 10$, the spectrum shows broad line components, but we confirm that all of the 18 galaxies meet $Q_f < 9$. We measure the LAE overdensity around these galaxies in basically the same manner as described in Sec. 3.2, by using 37 bright LAEs with $\text{NB816} < 24.5$, which corresponds to the limiting magnitudes of NB872 measured by a $2''.0$ diameter aperture in our observations. We evaluate $\langle \Sigma_{\text{LAE}} \rangle$ as $37/7056 = 0.005 \text{ arcmin}^{-2}$ in the COSMOS fields, where no quasars and no LAE protoclusters have been observed at $5.65 \leq z \leq 5.75$. While we do not correct the effect by masking low-quality regions, we regard the effect as relatively small (at most a factor of two based on the edge and mask region correction in our quasar fields) since the galaxies do not reside in the vicinity of the edge regions.

4.3.2 Do quasars affect the LAE overdensity?

Fig. 13 compares the LAE overdensities around our quasars with those of galaxies with a similar M_* . We find that the LAE overdensity of J0844–0132 is much stronger than that of any of the galaxies

¹⁰ <https://github.com/cosmosastro/speczcompilation>

¹¹ <https://cigale.lam.fr/>

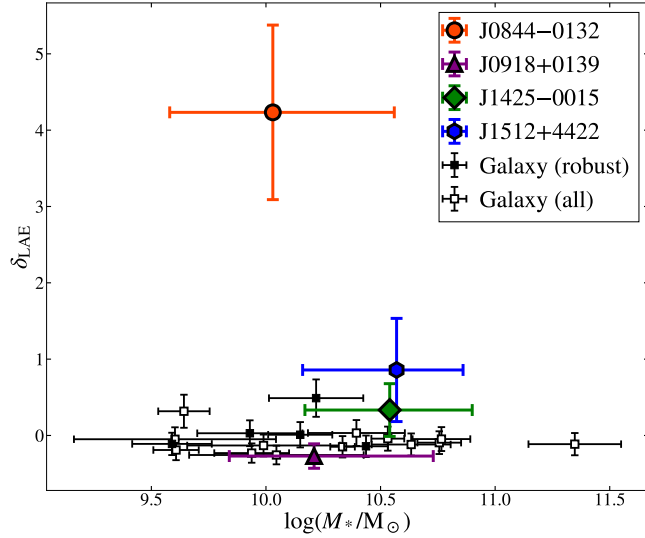


Figure 13. Comparison of surrounding LAE overdensities between our quasars and galaxies with similar M_* in the COSMOS field with a uniform threshold of $EW_0 > 25 \text{ \AA}$ selected to have $5.65 < z < 5.75$. The filled squares show the LAE overdensities of more robustly selected galaxies with reliable SED fitting and redshifts, while the open squares show those of all galaxies at $5.65 \leq z \leq 5.75$. The LAE overdensities are calculated in the manner described in Sec. 3.2.

with similar M_* , while the LAE overdensities in the remaining three quasars are comparable. This suggests that the LAE overdensities in the three regions fall within the range predicted from their M_* , with only J0844–0132 potentially exhibiting a distinctive overdensity. Assuming δ_{LAE} of galaxies follows a simple Gaussian distribution centred on zero, and the LAE overdensity $\delta_{\text{LAE}} = 4.23 \pm 1.14$ in J0844–0132 is an outlier at 3.7σ . The probability of this occurring is 2×10^{-4} , which is so small that it is unlikely to be considered a coincidence.

The strong overdensity of J0844–0132 implies that some quasars could enhance the galaxy formation around them, an effect opposite to the negative feedback from quasars (e.g. photoevaporation). Zana et al. (2022) use a cosmological simulation to demonstrate that quasar feedback can enhance the star formation activity up to a few cMpc scale. They suggest that the outflow from the quasar supplies gas to its surroundings, triggers shock waves that enhance star formation efficiency, making the quasar's vicinity a potential site for star formation. The surrounding galaxies affected by this positive feedback from quasars may increase their luminosity, possibly resulting in the galaxy overdensity. Positive feedback from quasars may also increase the intrinsic number of surrounding galaxies as they stimulate the star formation in the surrounding gas, although the positive feedback only works efficiently in the vicinity of quasars. Otherwise, it is still possible that J0844–0132 resides in a very massive DMH highly exceeding the empirical stellar-to-halo mass ratio due to its large scatter. To verify the scenario, radiation-hydrodynamical simulations with high spatial resolution and large box sizes are necessary to evaluate the quasar feedback on their surrounding galaxies more accurately. In addition, observing the outflows from quasars and investigating the galaxies (e.g. [C II] emitters) around the quasars displaying the sign of outflows is important to evaluate the impact of the quasar feedback from the observational aspect, which is possible by using ALMA.

4.4 Other interpretations

Since this study observes quasars at the last stage of the reionization epoch, the LAE-deficient regions may correspond to the neutral islands (Giri et al. 2019; Keating et al. 2020; Nasir & D’Aloisio 2020), where the local IGM happens to have a high H_1 fraction. These regions can reduce the observable $\text{Ly}\alpha$ emission, which may explain the quasars in non-overdense regions. However, it is unlikely that a quasar emitting intense radiation could coexist with these neutral islands. Moreover, as shown in Fig. 8 and mentioned in Sec. 4.1.2, there is no tendency for EW_0 to be small only where θ is small. Therefore, the influence of patchy reionization is implausible.

Recently, Fontanot et al. (2025) demonstrated that the distribution of surrounding galaxies around quasars can distinguish between triggering mechanisms contributing to the quasar ignition — a galaxy merger event and a galactic disk instability — using the PLANCK MILLENNIUM simulation and the semi-analytic model of GAlaxy Evolution and Assembly (GAEA; De Lucia et al. 2024). Thus, two distinct mechanisms for quasar triggering also provide a plausible scenario to explain the diversity of the quasar environments. In fact, only J0844–0132 has a companion galaxy that is the sign of a galaxy merger among our quasars (Ding et al. 2025). However, it is difficult to verify this scenario observationally since the triggering mechanisms for individual quasars are hardly distinguishable. Further theoretical approaches (e.g. large cosmological simulations) are necessary to test the relation between the quasar environment and its triggering mechanisms.

Moreover, while high- z quasars on average possess relatively high DMH masses of around $\sim 10^{12} \text{ M}_\odot$ (Arita et al. 2023; Eilers et al. 2024; Huang et al. 2026; Wang et al. 2026), their DMH mass distribution might be broad, and the variety of DMH masses may be creating diverse environments. Recently, Wang et al. (2026) investigate diverse environments of 25 luminous quasars at $z > 6.5$ to find that the distributions of line-of-sight velocities of [O III] emitters around quasars in overdense regions are similar to those in massive DMHs with $\sim 10^{13} \text{ M}_\odot$, while those around the other ASPIRE quasars are more consistent with those around DMHs with 5×10^{11} – 10^{12} M_\odot . These results support the scenario that the DMH mass distribution is broad. Further observations of many high- z quasar fields with various host galaxy and SMBH properties are necessary to understand their intrinsic environments. Even if the DMH mass remains the same, the assembly bias on galaxy distribution may be the driver to generate diversity. This bias also depends on the observed galaxy population, making approaches that measure the environment with other galaxy populations equally important. In this sense, the other galaxy population (e.g. [O III] emitter, $\text{H}\alpha$ emitter) survey around many high- z quasars is essential, which can be performed by JWST/NIRCam narrowband imaging or slitless spectroscopy (e.g. Wang et al. 2023). In addition, investigating dust-obscured galaxies or submillimetre galaxies invisible by rest-UV survey to evaluate more accurate galaxy overdensity, which can be observed by ALMA and Submillimetre Common-User Bolometer Array 2 on the James Clerk Maxwell Telescope.

Finally, increasing the sample size and expanding the survey area are important to overcome the cosmic variance. As shown in Table 4, $\langle \Sigma_{\text{LAE}} \rangle$ of our quasar fields varies probably due to the cosmic variance, while the limiting magnitudes slightly differ among the quasar fields. Therefore, it is also useful to perform narrowband imaging for more quasar fields with a larger effective area.

5 SUMMARY

This paper searches for LAEs surrounding four low-luminosity ($-24 < M_{1450} < -22$) quasars at $z \sim 6.18$ (J0844–0132, J0918+0139, J1425–0015, J1512+4422) with NB872 on Subaru/HSC to characterize their environments out to ~ 100 cMpc. These quasars are identified by the SHELLQs project and have been observed by JWST, unveiling the properties of their host galaxies (M_* , SFR, sSFR) and SMBHs (M_{BH} , bolometric luminosity, Eddington ratio). We select LAE candidates with the colour criteria of equations (4)–(7) and perform a careful visual inspection. We identified 88, 31, 28, and 23 LAEs in the fields of J0844–0132 (5173 arcmin 2), J0918+0139 (4837 arcmin 2), J1425–0015 (5092 arcmin 2), and J1512+4422 (5137 arcmin 2), respectively, not including the central quasars. The surface number density of LAEs > 50 cMpc away from the central quasars in our fields is almost comparable to that in blank fields at $z = 5.7$ and $z = 6.6$ (Kondo et al. 2018). We also compute the LAE overdensity using KDE with a Gaussian kernel, setting the bandwidth to 17.7 cMpc, the correlation length between galaxies and quasars at $z \sim 6$ (Arita et al. 2023). The main findings of this paper are summarized as follows:

(i) The J0844–0132 field exhibits a high LAE overdensity with $\delta_{\text{LAE}} = 3.77 \pm 0.97$ at the quasar position. The LAE overdensities of the three other quasar fields are consistent with zero within their 1σ uncertainty. These results are summarized in Fig. 7 and Table 4.

(ii) We measure their EW_0 based on the $z - \text{NB872}$ colour and verify whether EW_0 is correlated with the separation from the quasar (θ) by computing Kendall’s τ . The hypothesis testing suggests that EW_0 is independent of θ in all of our quasar fields.

(iii) We measure the proximity zone sizes of our quasars by applying QFA to their spectra. No LAEs are found within the proximity zones of our quasars. The absence of LAEs within the proximity zone of J0844–0132 is consistent with the expected number of LAEs based on Σ_{LAE} at the quasar position, making it difficult to verify whether the photoevaporation effect works efficiently. In the remaining three fields, LAE overdensities are not observed over the proximity zone sizes. Hence, we conclude that the absence of LAE overdensities in the three fields is not due to the photoevaporation effect. Our results, which show a broad environment from $\delta_{\text{LAE}} = 0.01$ to $\delta_{\text{LAE}} = 3.77$, indicate that the LAE density around the quasar exhibits diversity independent of the photoevaporation effect.

(iv) The proximity zone size of J0844–0132 is the smallest among our quasars ($R_p = 0.4449 \pm 0.0093$ pMpc), implying that it is a young quasar. If J0844–0132 is still young, it may suggest that even if photoevaporation works efficiently, it would not have sufficient time to inhibit star formation in surrounding galaxies by its intense radiation.

(v) None of the properties of the host galaxies (M_* , SFR, sSFR) or SMBHs (M_{BH} , bolometric luminosity, Eddington ratio) are found to be strongly related to the LAE overdensity contrary to expectations that galaxies with high M_* or high M_{BH} would reside in massive DMHs and thus should be detected in galaxy overdense regions. While it might be due to the small size of our sample and the projection effect, the discrepancy is caused by the large scatter between the DMH mass and the SMBH mass.

(vi) The mass-weighted age of the host galaxy of J1512+4422, which shows no significant LAE overdensity, is 150 Myr (Onoue et al. 2025). The age is significantly older than the typical age of an LAE ($\sim 1\text{--}3$ Myr). This suggests that even if a galaxy overdensity exists around the quasar, the surrounding galaxies may also be similarly old and show no significant Ly α emission.

(vii) We find that the LAE overdensity in the J0844–0132 field

is stronger than that of galaxies with similar M_* at $z \sim 6$, while the other quasar fields show a comparable LAE overdensity. The positive feedback from the quasar to promote the star formation activity of the surrounding galaxies may contribute to the large LAE overdensity in the field. However, the positive feedback works efficiently only up to a few cMpc scale; hence, it is also possible that the quasar resides in a very massive DMH exceeding the empirical stellar-to-halo mass ratio due to its large scatter.

(viii) The observed diversity of high- z quasar environments may also be attributed to different triggering channels, with mergers and galactic disk instabilities, of the quasar ignition or to the broad halo mass distribution.

This study demonstrates that the environments of high- z quasars are diverse. Nevertheless, it is highly intriguing that the DMH mass of high- z quasars remains nearly constant over cosmic time (Arita et al. 2023; Eilers et al. 2024; Huang et al. 2026; Wang et al. 2026). Furthermore, the observed diversity poses a significant challenge to many simulations that predict that high- z quasars ubiquitously reside in high-density regions. Even considering these factors, further observational constraints are necessary to fully understand the diverse quasar environments. The LAE selection in this work uses imaging observations with the narrowband filter NB872, which suggests spectroscopic follow-up to determine the precise three-dimensional LAE distribution in the quasar fields. The precise distribution will reveal a possible anisotropic quasar feedback and evaluate the accurate galaxy overdensity. Therefore, future spectroscopic follow-up by, for example, Prime Focus Spectrograph (PFS; Tamura et al. 2016) will be useful to determine their robust redshifts. Observing more quasar fields with a narrowband filter will be useful to statistically evaluate the quasar impact on its large-scale environments, but not all quasars have a narrowband filter that corresponds to their redshifts. To increase the sample size, slitless spectroscopy is suitable as it can identify galaxies around quasars without any target selection. For example, the upcoming JWST NIRCam Wide Field Slitless Spectroscopy mode observation (GO 7519; PI: J. Arita) will search for [O III] emitters around 12 SHELLQs quasars, including the targeted quasars in this paper. This observation will allow us to reveal the quasar environments, including the immediate vicinity of quasars, by using general star-forming galaxies. Although the FoV of NIRCam is much smaller than that of HSC, this observation enables us to directly compare the galaxy overdensity of quasars with that of normal galaxies with the same M_* and redshift range. These observational approaches will also enable us to verify the SMBH growth theory in the early Universe and help more sophisticated cosmological simulations.

ACKNOWLEDGEMENTS

We thank Linhua Jiang, Roberto Gilli, and Fabio Vito for constructive discussions. JA is supported by the Japan Society for the Promotion of Science (JSPS) KAKENHI grant number JP24KJ0858 and International Graduate Program for Excellence in Earth-Space Science (IGPEES), a World-leading Innovative Graduate Study (WINGS) Program, the University of Tokyo. NK is supported by the Japan Society for the Promotion of Science through Grant-in-Aid for Scientific Research 21H04490, 25H00663, 25K01038, 25K01044. YM is supported by the Japan Society for the Promotion of Science (JSPS) KAKENHI Grant No. 21H04494. MO is supported by the Japan Society for the Promotion of Science (JSPS) KAKENHI Grant Number 24K22894. SK is supported by the JSPS through Grant-in-Aid for Scientific Research 24KJ0058, 24K17101.

The Hyper Suprime-Cam (HSC) collaboration includes the astronomical communities of Japan and Taiwan, and Princeton University. The HSC instrumentation and software were developed by the National Astronomical Observatory of Japan (NAOJ), the Kavli Institute for the Physics and Mathematics of the Universe (Kavli IPMU), the University of Tokyo, the High Energy Accelerator Research Organization (KEK), the Academia Sinica Institute for Astronomy and Astrophysics in Taiwan (ASIAA), and Princeton University. Funding was contributed by the FIRST program from the Japanese Cabinet Office, the Ministry of Education, Culture, Sports, Science and Technology (MEXT), the Japan Society for the Promotion of Science (JSPS), Japan Science and Technology Agency (JST), the Toray Science Foundation, NAOJ, Kavli IPMU, KEK, ASIAA, and Princeton University.

This paper is based [in part] on data collected at the Subaru Telescope and retrieved from the HSC data archive system, which is operated by Subaru Telescope and Astronomy Data Center (ADC) at NAOJ. Data analysis was in part carried out with the cooperation of Center for Computational Astrophysics (CfCA) at NAOJ. We are honored and grateful for the opportunity of observing the Universe from Maunakea, which has the cultural, historical and natural significance in Hawaii.

This paper makes use of software developed for Vera C. Rubin Observatory. We thank the Rubin Observatory for making their code available as free software at <http://pipelines.lsst.io/>.

The Pan-STARRS1 Surveys (PS1) and the PS1 public science archive have been made possible through contributions by the Institute for Astronomy, the University of Hawaii, the Pan-STARRS Project Office, the Max Planck Society and its participating institutes, the Max Planck Institute for Astronomy, Heidelberg, and the Max Planck Institute for Extraterrestrial Physics, Garching, The Johns Hopkins University, Durham University, the University of Edinburgh, the Queen's University Belfast, the Harvard-Smithsonian Center for Astrophysics, the Las Cumbres Observatory Global Telescope Network Incorporated, the National Central University of Taiwan, the Space Telescope Science Institute, the National Aeronautics and Space Administration under grant No. NNX08AR22G issued through the Planetary Science Division of the NASA Science Mission Directorate, the National Science Foundation grant No. AST-1238877, the University of Maryland, Eotvos Lorand University (ELTE), the Los Alamos National Laboratory, and the Gordon and Betty Moore Foundation.

DATA AVAILABILITY

The data in this paper will be shared upon reasonable requests to the corresponding author.

REFERENCES

Abdurro'uf et al., 2022, *ApJS*, **259**, 35

Aihara H., et al., 2018, *PASJ*, **70**, S4

Arita J., et al., 2023, *ApJ*, **954**, 210

Arita J., Kashikawa N., Onoue M., Yoshioka T., Takeda Y., Hoshi H., Shimizu S., 2025, *MNRAS*, **536**, 3677

Bañados E., Venemans B., Walter F., Kurk J., Overzier R., Ouchi M., 2013, *ApJ*, **773**, 178

Bañados E., et al., 2014, *AJ*, **148**, 14

Bañados E., et al., 2016, *ApJS*, **227**, 11

Bañados E., et al., 2018, *Nature*, **553**, 473

Balmaverde B., et al., 2017, *A&A*, **606**, A23

Barkana R., Loeb A., 1999, *ApJ*, **523**, 54

Behroozi P. S., Wechsler R. H., Conroy C., 2013, *ApJ*, **770**, 57

Behroozi P., Wechsler R. H., Hearn A. P., Conroy C., 2019, *MNRAS*, **488**, 3143

Bertin E., 2011, in Evans I. N., Accomazzi A., Mink D. J., Rots A. H., eds, *Astronomical Society of the Pacific Conference Series* Vol. 442, *Astronomical Data Analysis Software and Systems XX*. p. 435

Blanc G. A., et al., 2008, *ApJ*, **681**, 1099

Boquien M., Burgarella D., Roehlly Y., Buat V., Ciesla L., Corre D., Inoue A. K., Salas H., 2019, *A&A*, **622**, A103

Bosch J., et al., 2018, *PASJ*, **70**, S5

Bosman S. E. I., Kakiuchi K., Meyer R. A., Gronke M., Laporte N., Ellis R. S., 2020, *ApJ*, **896**, 49

Bunker A. J., Warren S. J., Hewett P. C., Clements D. L., 1995, *MNRAS*, **273**, 513

Carilli C. L., et al., 2010, *ApJ*, **714**, 834

Carranza-Escudero M., et al., 2025, *ApJ*, **989**, L50

Cen R., Haiman Z., 2000, *ApJ*, **542**, L75

Chambers K. C., et al., 2016, *arXiv e-prints*, p. arXiv:1612.05560

Champagne J. B., et al., 2025, *ApJ*, **981**, 113

Clarke L., Shapley A. E., Sanders R. L., Topping M. W., Brammer G. B., Bento T., Reddy N. A., Kehoe E., 2024, *ApJ*, **977**, 133

Cooke E. A., Hatch N. A., Muldrew S. I., Rigby E. E., Kurk J. D., 2014, *MNRAS*, **440**, 3262

Costa T., Sijacki D., Trenti M., Haehnelt M. G., 2014, *MNRAS*, **439**, 2146

Coupon J., Czakon N., Bosch J., Komiyama Y., Medezinski E., Miyazaki S., Oguri M., 2018, *PASJ*, **70**, S7

Croom S. M., et al., 2005, *MNRAS*, **356**, 415

Curran P. A., 2014, *arXiv e-prints*, p. arXiv:1411.3816

Davies F. B., Hennawi J. F., Eilers A.-C., 2020, *MNRAS*, **493**, 1330

De Lucia G., Fontanot F., Xie L., Hirschmann M., 2024, *A&A*, **687**, A68

Decarli R., et al., 2018, *ApJ*, **854**, 97

Ding X., et al., 2023, *Nature*, **621**, 51

Ding X., et al., 2025, *ApJ*, **993**, 91

Dubois Y., et al., 2014, *MNRAS*, **444**, 1453

Eilers A.-C., Davies F. B., Hennawi J. F., Prochaska J. X., Lukić Z., Mazzucchelli C., 2017, *ApJ*, **840**, 24

Eilers A.-C., et al., 2024, *ApJ*, **974**, 275

Fan X., et al., 2006, *AJ*, **132**, 117

Fan X., Bañados E., Simcoe R. A., 2023, *ARA&A*, **61**, 373

Farina E. P., et al., 2017, *ApJ*, **848**, 78

Farina E. P., et al., 2022, *ApJ*, **941**, 106

Fei Q., et al., 2025, *ApJ*, **980**, 84

Fontanot F., Decarli R., De Lucia G., Cucciati O., Xie L., Hirschmann M., 2025, *arXiv e-prints*, p. arXiv:2511.15789

Furusawa H., et al., 2018, *PASJ*, **70**, S3

Gaia Collaboration et al., 2016, *A&A*, **595**, A1

Gaia Collaboration et al., 2023, *A&A*, **674**, A1

Giri S. K., Mellema G., Aldheimer T., Dixon K. L., Iliev I. T., 2019, *MNRAS*, **489**, 1590

Goto T., Utsumi Y., Kikuta S., Miyazaki S., Shiki K., Hashimoto T., 2017, *MNRAS*, **470**, L117

Granato G. L., De Zotti G., Silva L., Bressan A., Danese L., 2004, *ApJ*, **600**, 580

Habouzit M., Volonteri M., Somerville R. S., Dubois Y., Peirani S., Pichon C., Devriendt J., 2019, *MNRAS*, **489**, 1206

Hatch N. A., Kurk J. D., Pentericci L., Venemans B. P., Kuiper E., Miley G. K., Röttgering H. J. A., 2011, *MNRAS*, **415**, 2993

Huang J., et al., 2026, *arXiv e-prints*, p. arXiv:2602.04974

Inayoshi K., 2025, *ApJ*, **988**, L22

Ishimoto R., et al., 2020, *ApJ*, **903**, 60

Isobe T., Feigelson E. D., Nelson P. I., 1986, *ApJ*, **306**, 490

Ito K., et al., 2021, *ApJ*, **916**, 35

Jiang L., et al., 2006, *AJ*, **132**, 2127

Jiang L., et al., 2013, *ApJ*, **772**, 99

Jiang L., et al., 2018, *Nature Astronomy*, **2**, 962

Jones M. C., 1993, *Statistics and Computing*, **3**, 135

Kashikawa N., et al., 2002, *PASJ*, **54**, 819

Kashikawa N., Kitayama T., Doi M., Misawa T., Komiyama Y., Ota K., 2007, *ApJ*, **663**, 765

Kashino D., Lilly S. J., Matthee J., Eilers A.-C., Mackenzie R., Bordoloi R., Simcoe R. A., 2023, *ApJ*, **950**, 66

Kashino D., et al., 2026, *ApJ*, **997**, 280

Kaspi S., Smith P. S., Netzer H., Maoz D., Jannuzzi B. T., Giveon U., 2000, *ApJ*, **533**, 631

Kawanomoto S., et al., 2018, *PASJ*, **70**, 66

Keating L. C., Weinberger L. H., Kulkarni G., Haehnelt M. G., Chardin J., Aubert D., 2020, *MNRAS*, **491**, 1736

Kennicutt R. C., Evans N. J., 2012, *ARA&A*, **50**, 531

Khostovan A. A., et al., 2026, *ApJS*, **282**, 6

Kikuta S., Imanishi M., Matsuoka Y., Matsuda Y., Shimasaku K., Nakata F., 2017, *ApJ*, **841**, 128

Kim S., et al., 2009, *ApJ*, **695**, 809

Kocevski D. D., et al., 2025, *ApJ*, **986**, 126

Komiyama Y., et al., 2018, *PASJ*, **70**, S2

Konno A., et al., 2018, *PASJ*, **70**, S16

Koyama Y., et al., 2013, *MNRAS*, **434**, 423

Kurk J. D., et al., 2007, *ApJ*, **669**, 32

Lambert T. S., et al., 2024, *A&A*, **689**, A331

Lawrence A., et al., 2007, *MNRAS*, **379**, 1599

Li Q., et al., 2020, *ApJ*, **900**, 12

Lin X., et al., 2025, arXiv e-prints, p. arXiv:2505.02896

Madau P., 1995, *ApJ*, **441**, 18

Maiolino R., et al., 2005, *A&A*, **440**, L51

Martini P., Weinberg D. H., 2001, *ApJ*, **547**, 12

Matsuoka Y., et al., 2016, *ApJ*, **828**, 26

Matsuoka Y., et al., 2018a, *PASJ*, **70**, S35

Matsuoka Y., et al., 2018b, *ApJS*, **237**, 5

Matsuoka Y., et al., 2019a, *ApJ*, **872**, L2

Matsuoka Y., et al., 2019b, *ApJ*, **883**, 183

Matsuoka Y., et al., 2025, *ApJ*, **988**, 57

Mazzucchelli C., Bañados E., Decarli R., Farina E. P., Venemans B. P., Walter F., Overzier R., 2017, *ApJ*, **834**, 83

Mignoli M., et al., 2020, *A&A*, **642**, L1

Miyazaki S., et al., 2018, *PASJ*, **70**, S1

Morselli L., et al., 2014, *A&A*, **568**, A1

Mortlock D. J., et al., 2011, *Nature*, **474**, 616

Nasir F., D’Aloisio A., 2020, *MNRAS*, **494**, 3080

Oke J. B., Gunn J. E., 1983, *ApJ*, **266**, 713

Ono Y., Ouchi M., Shimasaku K., Dunlop J., Farrah D., McLure R., Okamura S., 2010, *ApJ*, **724**, 1524

Onoue M., et al., 2025, *Nature Astronomy*, **9**, 1541

Ota K., et al., 2018, *ApJ*, **856**, 109

Overzier R. A., 2022, *ApJ*, **926**, 114

Overzier R. A., Guo Q., Kauffmann G., De Lucia G., Bouwens R., Lemson G., 2009, *MNRAS*, **394**, 577

Peirani S., et al., 2017, *MNRAS*, **472**, 2153

Phillips C. L., et al., 2025, arXiv e-prints, p. arXiv:2510.22403

Pizzati E., et al., 2024, *MNRAS*, **534**, 3155

Prieto-Lyon G., et al., 2025, arXiv e-prints, p. arXiv:2509.18302

Privon G. C., et al., 2020, *ApJ*, **893**, 149

Protušová K., et al., 2025, *A&A*, **700**, A218

Pudoka M., et al., 2024, *ApJ*, **968**, 118

Quadri R., et al., 2007, *AJ*, **134**, 1103

Richards G. T., et al., 2006, *ApJS*, **166**, 470

Rowe B. T. P., et al., 2015, *Astronomy and Computing*, **10**, 121

Runnoe J. C., Brotherton M. S., Shang Z., 2012, *MNRAS*, **422**, 478

Salmon B., et al., 2015, *ApJ*, **799**, 183

Santos S., Sobral D., Matthee J., 2016, *MNRAS*, **463**, 1678

Schaerer D., 2003, *A&A*, **397**, 527

Schindler J.-T., et al., 2025, *Nature Astronomy*, **9**, 1732

Scoville N., et al., 2007, *ApJS*, **172**, 1

Serjeant S., et al., 2000, *MNRAS*, **316**, 768

Shen Y., et al., 2009, *ApJ*, **697**, 1656

Shen Y., et al., 2019, *ApJ*, **873**, 35

Shibata K., et al., 2025, *ApJ*, **993**, 42

Shibuya T., Ouchi M., Harikane Y., 2015, *ApJS*, **219**, 15

Shibuya T., et al., 2018, *PASJ*, **70**, S14

Simpson C., Mortlock D., Warren S., Cantalupo S., Hewett P., McLure R., McMahon R., Venemans B., 2014, *MNRAS*, **442**, 3454

Sobral D., Smail I., Best P. N., Geach J. E., Matsuda Y., Stott J. P., Cirasuolo M., Kurk J., 2013, *MNRAS*, **428**, 1128

Springel V., et al., 2005, *Nature*, **435**, 629

Sun Z., Ting Y.-S., Cai Z., 2023, *ApJS*, **269**, 4

Suzuki Y., et al., 2024, *ApJ*, **972**, 82

Suzuki Y., Matsuoka Y., Kikuta S., Uchiyama H., Kusakabe H., Imanishi M., 2025, *ApJ*, **995**, L31

Tamura N., et al., 2016, in Evans C. J., Simard L., Takami H., eds, Society of Photo-Optical Instrumentation Engineers (SPIE) Conference Series Vol. 9908, Ground-based and Airborne Instrumentation for Astronomy VI. p. 99081M (arXiv:1608.01075), doi:10.1117/12.2232103

Uchiyama H., et al., 2018, *PASJ*, **70**, S32

Uchiyama H., et al., 2019, *ApJ*, **870**, 45

Uchiyama H., et al., 2020, *ApJ*, **905**, 125

Utsumi Y., Goto T., Kashikawa N., Miyazaki S., Komiyama Y., Furusawa H., Overzier R., 2010, *ApJ*, **721**, 1680

Venemans B. P., McMahon R. G., Warren S. J., Gonzalez-Solares E. A., Hewett P. C., Mortlock D. J., Dye S., Sharp R. G., 2007, *MNRAS*, **376**, L76

Venemans B. P., et al., 2013, *ApJ*, **779**, 24

Venemans B. P., et al., 2015, *ApJ*, **801**, L11

Verro K., et al., 2022, *A&A*, **660**, A34

Vestergaard M., Osmer P. S., 2009, *ApJ*, **699**, 800

Vestergaard M., Peterson B. M., 2006, *ApJ*, **641**, 689

Volonteri M., Rees M. J., 2006, *ApJ*, **650**, 669

Wang F., Wang R., Fan X., Wu X.-B., Yang J., Neri R., Yue M., 2019a, *ApJ*, **880**, 2

Wang F., et al., 2019b, *ApJ*, **884**, 30

Wang F., et al., 2021, *ApJ*, **907**, L1

Wang F., et al., 2023, *ApJ*, **951**, L4

Wang F., et al., 2024, *ApJ*, **962**, L11

Wang F., et al., 2026, arXiv e-prints, p. arXiv:2602.04979

Willott C. J., Percival W. J., McLure R. J., Crampton D., Hutchings J. B., Jarvis M. J., Sawicki M., Simard L., 2005, *ApJ*, **626**, 657

Willott C. J., et al., 2007, *AJ*, **134**, 2435

Willott C. J., et al., 2010, *AJ*, **140**, 546

Yang G., et al., 2020a, *MNRAS*, **491**, 740

Yang J., et al., 2020b, *ApJ*, **897**, L14

Yang J., et al., 2021, *ApJ*, **923**, 262

Yue M., et al., 2024, *ApJ*, **966**, 176

Zana T., Gallerani S., Carniani S., Vito F., Ferrara A., Lupi A., Di Mascia F., Barai P., 2022, *MNRAS*, **513**, 2118

Zheng W., et al., 2006, *ApJ*, **640**, 574

APPENDIX A: SELECTION COMPLETENESS OF THE COLOUR SELECTION CRITERIA

We compute the selection completeness of our selection criteria, which is defined as the recovery rate of LAEs within a given EW_0 range that are selected by our colour selection. We assume the same intrinsic EW_0 distribution as [Shibuya et al. \(2018\)](#) obtained at $z = 5.7$:

$$\frac{dN}{d\text{EW}_0} = N \exp\left(-\frac{\text{EW}_0}{W_e}\right), \quad (\text{A1})$$

where W_e is the Ly α EW_0 scale length of the exponential function. We set W_e to 138 Å from the results at $z = 5.7$ ([Shibuya et al. 2018](#)). Following the EW_0 distribution, we generate 1000 mock LAEs with $\alpha = -2.5$ and FWHM of 250 km s $^{-1}$ for each redshift bin between $z = 6.12$ to $z = 6.23$ with a step of $\Delta z = 0.001$. We compute the selection completeness of LAEs with three EW_0 ranges:

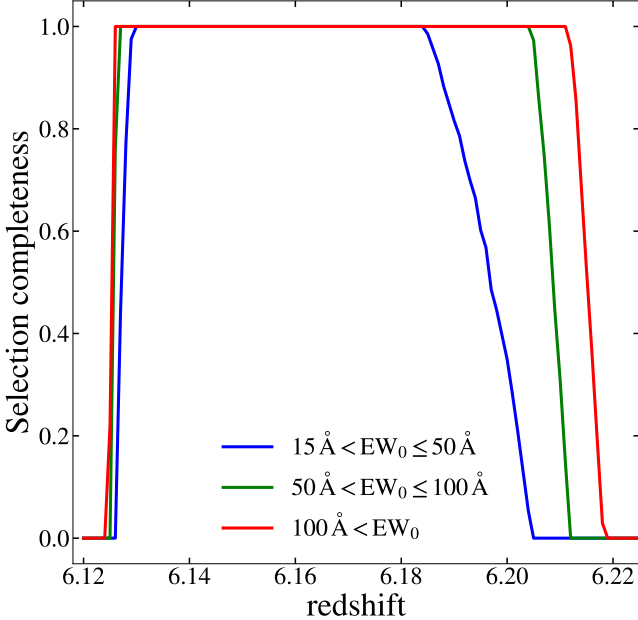


Figure A1. Selection completeness of our colour selection criteria as a function of redshift. The colour shows the EW_0 ranges of LAEs.

$15 \text{ \AA} < \text{EW}_0 \leq 50 \text{ \AA}$, $50 \text{ \AA} < \text{EW}_0 \leq 100 \text{ \AA}$, and $100 \text{ \AA} < \text{EW}_0$. Their selection completeness is shown in Fig. A1. We find that our selection criteria can sufficiently select the LAEs at our quasars' redshifts.

APPENDIX B: RELATION BETWEEN GALAXY OVERDENSITY AND THE PROPERTIES OF THE HOST GALAXY AND SMBH

In Sec. 4.2, we investigate the relation between LAE overdensity and the properties of the host galaxy and SMBH. Recently, the EIGER and ASPIRE projects have represented results on [O III] emitter overdensity around high- z quasars. Since the bias parameter could differ across galaxy populations and the spatial coverage for measuring overdensity varies between telescopes, a simple comparison between the two carries inherent risks. Furthermore, the methods for measuring M_* and SFR also differ between studies. However, considering the limited number of samples available to investigate this correlation, we present the results in Fig. B1 and Fig. B2, which include these [O III] emitter samples, for reference purposes with the aim of increasing the sample size as much as possible. Readers should treat these results as purely indicative.

Among the EIGER and ASPIRE quasars, except those in Table 5, four EIGER quasars have their M_* and SFR measured: SDSS J010013.02+260225.8 (hereafter J0100+2802) at $z = 6.33$; ULAS J014837.63+060020.0 (hereafter J0148+0600) at $z = 5.98$; SDSS J114816.65+525150.2 (hereafter J1148+5251) at $z = 6.42$; PSO J159.2257–02.5438 (hereafter J159–02) at $z = 6.38$, whose redshifts are from Kashino et al. (2026). Their M_* is measured by Yue et al. (2024) using the same method for J1030+0524. The SFRs of J0100+2802, J0148+0600, J1148+5251, and J159–02 are evaluated in Wang et al. (2019a), Li et al. (2020), Maiolino et al. (2005), and Decarli et al. (2018), respectively. To infer the SFRs, Maiolino et al. (2005) use the [C II] line luminosity, and the others use FIR

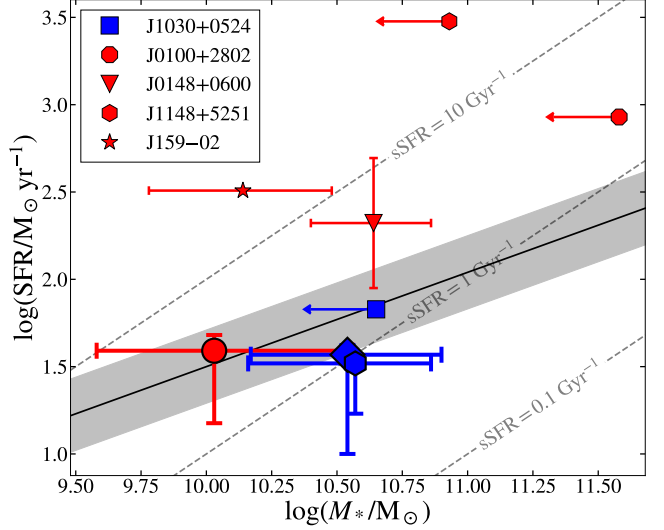


Figure B1. The relationship between M_* and the SFR of the quasars. The plots for J0100+2802, J1148+5251, and J159–02 are added to Fig. 11. The red and blue symbols of the EIGER quasars show that the quasars reside in the overdense and non-overdense regions of [O III] emitters, respectively.

luminosity. The overdensities of [O III] emitters for the first three quasars and J1030+0524 are measured in Eilers et al. (2024). They show that the observed overdensities within a radius of 2 cMpc around J0100+2802, J0148+0600, J1148+5251, and J1030+0524 are 29 ± 10 , 65 ± 15 , 16 ± 8 , and 3 ± 4 , respectively. This result suggests that J1030+0524 resides in a non-overdense region of [O III] emitters while the other quasars reside in overdense regions. While the overdensity around J159–02 is not evaluated in Eilers et al. (2024), Kashino et al. (2026) shows that the number of [O III] emitters in the J159–02 field has a peak at the quasar redshift. Therefore, we consider that J159–02 resides in an overdense field of [O III] emitters. In addition, LBG overdensities around some of the quasars have also been measured. Pudoka et al. (2024) show that the LBG overdensity of the J0100+2802 field is $\delta = 4$ at 8.4σ . Morselli et al. (2014) evaluate the LBG overdensity of the J1148+5251 and J1030+0524 fields as $\delta = 0.9$ and 2.0 with the significance of $\sigma_\delta = 1.9$ and 3.3 , respectively. These studies reveal that J0100+2802 and J1148+5251 reside in galaxy overdensities of both [O III] emitters and LBGs, but that the J1030+0524 field does not show an overdensity of [O III] emitters despite representing the LAE and LBG overdensities.

Fig. B1 shows the relationship between M_* and the SFR of the quasars with that of our quasars. Our quasars lie on the main sequence, whereas four quasars from the newly added EIGER quasars show starburst-like high SFRs above the main sequence, and all exhibit OIII emitter overdensities. While this result is highly intriguing, it is difficult to immediately conclude a correlation between the overdensity and the SFR or sSFR of the quasar host galaxies. This is due to the heterogeneous sample consisting of LAEs and [O III] emitters, the differences in volume used to measure the overdensity, the lack of uniformity in the SFR measurement methods, and the still limited data on the SFR and M_* of the host galaxies.

Regarding the SMBH properties, all of the EIGER and ASPIRE quasars have their M_{BH} and bolometric luminosities measured from spectroscopic observations by JWST. We refer to the measurements in Yue et al. (2024) and Wang et al. (2026) and the overdensity of [O III] emitters in Eilers et al. (2024) and Wang et al. (2026) for the

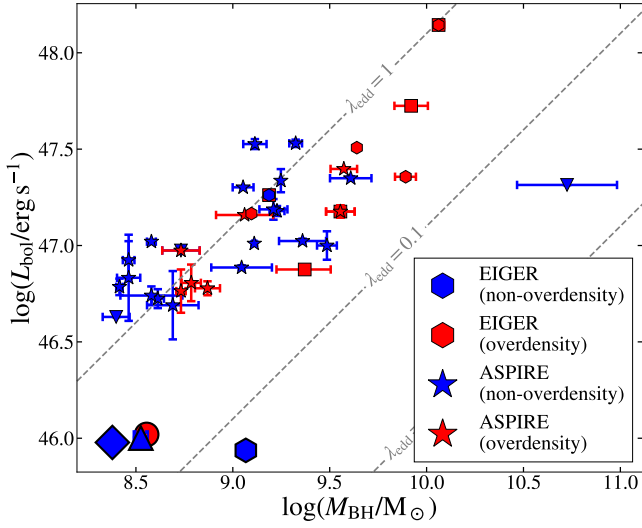


Figure B2. The SMBH masses and the bolometric luminosities of the quasars. The plots for the EIGER and ASPIRE quasars are added to Fig. 12. The red and blue symbols of the EIGER quasars show that the quasars reside in the overdense and non-overdense regions of [O III] emitters, respectively.

EIGER and ASPIRE quasars, respectively. Among the EIGER and ASPIRE quasars, one and seven quasars out of five and 25 quasars reside in the overdense regions of [O III] emitters.

Fig. B2 shows the relationship between M_{BH} and the bolometric luminosity of the EIERG and ASPIRE quasars in addition to those in Fig. 12. Even after adding the EIGER and ASPIRE quasars to those in Sec. 4.2.2, no correlations between galaxy overdensity and SMBH properties are confirmed.

This paper has been typeset from a $\text{\TeX}/\text{\LaTeX}$ file prepared by the author.